

1 **Revision 1:**

2 **Tourmaline and zircon trace the nature and timing of magmatic-hydrothermal**  
3 **episodes in granite-related Sn mineralization: Insights from the Libata Sn ore**  
4 **field**

5 *Victor Ikechukwu Vincent<sup>1,2</sup>, Huan Li<sup>2\*</sup>, Musa Bala Girei<sup>2,3,4</sup>, Michael W. Förster<sup>5</sup>, Vandi Dlama*  
6 *Kamaunji<sup>1</sup>*

7 *1. Faculty of Earth Sciences, China University of Geosciences, 430074, Wuhan, P.R. China*

8 *2. Key Laboratory of Metallogenic Prediction of Nonferrous Metals and Geological Environment*  
9 *Monitoring, Ministry of Education, School of Geosciences and Info-Physics, Central South*  
10 *University, Changsha 410083, China*

11 *3. Faculty of Earth Resources, State Key Laboratory of Geological Processes and Mineral*  
12 *Resources, China University of Geosciences, Wuhan 430074, China*

13 *4. Department of Geology, Bayero University Kano, Kano State, Nigeria*

14 *5. Department of Earth and Environmental Sciences, Macquarie University, NSW 2109, Sydney,*  
15 *Australia*

16 *\*Corresponding author (H. Li): [lihuan@csu.edu.cn](mailto:lihuan@csu.edu.cn)*

17 **ABSTRACT**

18 The Bin Yauri-Libata polymetallic ore district is a Sn and Au ore-bearing district in the Zuru schist  
19 belt, Northwestern Nigeria. The Libata Sn ore field is characterized by a set of cassiterite-bearing  
20 hydrothermal veins associated with Neoproterozoic Pan-African granites affected by deformation  
21 and low-grade metamorphism. The hydrothermal alteration associated with cassiterite-bearing

22 quartz veins in the Libata deposit includes silicification, albitization, chloritization, and potassic  
23 alteration. In this study, geochemical and geochronological data from tourmalines and zircons  
24 from Sn bearing lodes, unmineralized and altered granites is applied to reveal the timing, fluid  
25 composition, and source of ore-forming materials for tin mineralization in the Libata ore field.  
26 Zircon trace element and Hf isotopes ( $\epsilon\text{Hf}(t) = +4.37$  to  $+10.85$ ) reveal a mantle-derived source  
27 with some crustal contribution for the melts forming the Libata Sn-bearing granites. LA-ICPMS  
28 zircon U-Pb dating constrains the magmatic and hydrothermal ages to 650-646 Ma and 649-646  
29 Ma for the Libata granites. Overlapping zircon  $\epsilon\text{Hf}(t)$  and  $^{176}\text{Hf}/^{177}\text{Hf}$  but distinct  $^{176}\text{Lu}/^{177}\text{Hf}$  and  
30  $^{176}\text{Yb}/^{177}\text{Hf}$  ratios from magmatic and hydrothermally altered zircons reveal a magmatic source for  
31 the hydrothermal fluids which triggered cassiterite deposition in the Libata ore field. Major  
32 element chemistry constrain tourmalines from the Libata ore field as schorls that show high alkalis,  
33 low Ca contents, and moderate  $x$  values (where  $x$  is x-site vacancy). High Li, Zn, and Sn  
34 concentrations in tourmaline as well as Li/Sr and Ca-Fe-Mg ratios demonstrate that the tourmaline  
35 formed from granite-sourced fluid likely derived from the host Libata granites. Measured  $\delta^{11}\text{B}$   
36 values from the Libata tourmaline range from  $-15.69\text{‰}$  to  $-14.07\text{‰}$ . The  $\delta^{11}\text{B}$  of the mineralizing  
37 fluid is estimated to be  $-13.1$  to  $-11.9\text{‰}$  for the Libata tourmalines at  $400\text{--}500\text{ °C}$  and overlaps  
38 with averages from fractionated granites worldwide. Therefore, our data show that tourmaline and  
39 zircon are useful tracers of magmatic-hydrothermal evolution in rare metal bearing granites  
40 systems.

41 **Keywords:** Tourmaline chemistry, Sn mineralization, Hydrothermally-altered zircons, Pan-  
42 African granites, B isotopes, Libata

## 43 INTRODUCTION

44 Tourmaline, an accessory mineral in various rock types, is common in most granitic rocks  
45 and in various types of hydrothermal ore deposits (Dutrow and Henry, 2011; Marschall and Jiang,  
46 2011). Due to its resistance to weathering and stability over a wide range of P-T-X conditions,  
47 tourmaline typically preserves geological information about the magma or hydrothermal fluid from  
48 which it precipitated (Marks et al., 2013). Since tourmaline incorporates a large variety of elements  
49 into its crystal lattice, hydrothermal tourmaline is a robust tools for tracking the nature and

50 evolution of mineralizing fluids in magmatic-hydrothermal systems (Jiang et al., 2004; Zhao et al.,  
51 2021a). Similarly, boron isotopes of tourmaline are a reliable tracer for fluid–rock interactions,  
52 boron sources, and fluid evolution in ore deposit systems (Yang et al., 2015; Codeço et al., 2017;  
53 Trumbull et al., 2019; Trumbull et al., 2020).

54 Zircon, a prevalent accessory phase in various rock types, is of increasing geological focus  
55 due to its resilience to weathering and ability to record geochronological, isotopic, and  
56 geochemical changes in host rocks (Hoskin, 2005; Valley et al., 2010). Trace element variations  
57 in zircon track magma evolution, metamorphism, and can serve as good recorders of magmatic-  
58 hydrothermal evolution in granitic systems (Claiborne et al., 2010; Li et al., 2014). The coupled  
59 use of zircon trace element composition, zircon Lu-Hf isotopes, and high-precision zircon U-Pb  
60 geochronology have been recognized as robust tools for tracking the timing and evolution of  
61 magmatic-hydrothermal stages in granite hosted ore deposits (Li et al., 2018; Jiang et al., 2020;  
62 Vincent et al., 2021).

63 Sn-W bearing lodes from Nigeria have long been a source of research and economic  
64 interest due to their abundance and world-class deposit styles (Girei et al., 2019). However, most  
65 of the present and historic mining has been from deposits associated with anorogenic ring  
66 complexes in northcentral Nigeria (Kinnaird and Bowden, 1987; Melcher et al., 2015). Deposits  
67 sourced from I- and S-type granitoids, pegmatites and other vein-type Sn deposits account for only  
68 5% of the production from Nigeria (Olade, 2021). These Sn-bearing granitoids, rare metal  
69 pegmatites, and vein-type deposits are primarily concentrated along a 500 km NE-SW trending  
70 belt (Fig. 1b) from the southwestern part of Nigeria to the Jos Plateau (Okunlola and Ocan, 2009;  
71 Adetunji et al., 2016). However, recent studies suggest a wider distribution range for the ore-  
72 bearing calc-alkaline granitic suites and pegmatites in Northwestern and Southeastern Nigeria

73 (Garba, 2003; Ero and Ekwueme, 2009). The cassiterite-tourmaline assemblages in quartz from  
74 the Libata deposit are similar to other granite-related Sn deposits found in Pan-African terrains of  
75 West Africa (Kinnaird et al., 2016). However, the timing, nature, and source of ore forming  
76 materials for these Sn-bearing granites remain poorly constrained. Therefore, a comprehensive  
77 geologic, geochemical, and isotopic study of the Libata Sn deposit is crucial in constraining the  
78 nature, genetic type, and genesis of Sn-bearing granites and vein systems in Northwestern Nigeria  
79 and by extension the Pan-African suites of the Nigeria-Benin Shield.

80 In this study, cassiterite-bearing lodes associated with granites in northwestern Nigeria  
81 were selected to evaluate the Sn mineralization history for these granites. This study presents  
82 textural observations together with zircon U-Pb age, zircon Lu-Hf isotope, tourmaline major-trace  
83 element and boron isotopic data from barren and mineralized granites to determine the origin and  
84 timing of magmatic and hydrothermal processes that are associated with Sn mineralization in the  
85 Libata ore field.

## 86 **GEOLOGICAL BACKGROUND**

87 The Nigeria basement complex forms part of the Trans-Saharan orogenic belt (Fig. 1a)  
88 extending from the Hoggar Massifs into West Africa (Cahen et al., 1984). Tectonic welding of the  
89 West African craton, Congo craton, and Pharusian belt between 700 to 590 Ma is interpreted to  
90 have formed the Trans-Saharan orogenic belt (Bute et al., 2019). The basement complex rocks of  
91 Northwestern Nigeria exhibit signatures of the Liberian, Eburnian, and Kibaran orogeny (Turner,  
92 1983). Based on differing lithology and tectonic evolution, the Nigerian basement complex is  
93 subdivided into a western and eastern terrain (Fig. 1b; Bute et al., 2019; Ferré et al., 1996). The  
94 basement complex rocks of the eastern terrain have witnessed significantly higher grades of  
95 metamorphism than those of the western terrain and are composed of gneisses, migmatites, and

96 metapelites (Ferré et al., 1996; Ferré et al., 1998). The country rocks of the western terrain are  
97 overlain by an array of N-S trending metasediments (Turner, 1983). Based on variations in  
98 metamorphic grade and lithology, several workers have proposed two distinct sets of  
99 metasediments, namely the “Older Metasediments” and “Younger Metasediments” (McCurry,  
100 1971). The grade of metamorphism is highest in the Older Metasediments where amphibolite  
101 metamorphic grade rocks, which formed around 2.5 Ga, have been reported (Turner, 1983). The  
102 Younger Metasediments are composed of fine to coarse-grained clastic deposits in largely  
103 undeformed structures of late Pan-African age (Turner, 1983). Extensive post-collisional (Pan-  
104 African) granitoid plutons, generated during the main to late-stages of the Pan-African orogeny  
105 (750-550 Ma), are widespread in the Older Metasediments of the eastern and western basement  
106 complex terrains (Ferré et al., 1996). The basement complex rocks are further intruded by later  
107 staged Carboniferous to early Cretaceous granites (324-141 Ma) termed “Younger Granites” to  
108 differentiate them from the more widely distributed “Older granites” of Pan-African (750-550 Ma)  
109 ages (Bute et al., 2019; Vincent et al., 2022).

## 110 **GEOLOGY OF THE LIBATA SN ORE FIELD**

111 The Libata area is composed of low-lying gneisses intruded by Pan-African granite  
112 porphyries and porphyritic biotite granites. The granitic rocks also intrude biotite-muscovite  
113 schists of the Zuru schist belt (Fig. 2a). The biotite-muscovite schists of the Zuru-Libata area show  
114 varying degrees of metamorphism with locally well-banded textures and gradation into hornfels  
115 (Danbatta and Garba, 2007). Two prominent Sn-bearing ore bodies have been found in the Libata  
116 ore field (Fig. 2b). Both Sn-bearing ore bodies in the Libata ore field are quartz veins with  
117 alteration zones bounding wall rocks. Vein 1 is a granite-hosted ore-bearing lode, while, vein 2 is  
118 a NE-SW trending metasedimentary-hosted ore-bearing lode (Fig. 2b). Wall rock samples from

119 the granite-hosted vein primarily consist of quartz, plagioclase, tourmaline, and minor biotite, with  
120 accessory albite, chlorite, and zircon (Figs. 3b; 4a). The main ore mineral is cassiterite, which is  
121 accompanied by minor sulfides such as pyrite. Gangue minerals include chlorite, tourmaline, and  
122 quartz. Cassiterite occurs primarily in the tourmaline-quartz veins and the adjacent tourmaline-  
123 bearing wall rocks. Based on the above observations, mineral paragenesis from ore-bearing veins  
124 in the Libata ore field are summarized in Fig. 5. The Libata ore field is also comprised of several  
125 alluvial Au workings (Fig. 2b). Elsewhere, tourmaline-bearing auriferous quartz veins are hosted  
126 in the metasediments of the Zuru schist belt (Fig. 2a) along fault zones at Bin Yauri and (Garba,  
127 2000).

## 128 **SAMPLING AND PETROGRAPHY**

129 Samples for zircon geochemistry and U-Pb dating analysis were collected from two  
130 outcrop samples representing unmineralized Pan-African granitoids (sample CR-01 – granite  
131 porphyry) and altered wall rocks near vein 1 (sample KB-01 – altered biotite granite) from the  
132 Libata Sn ore field. Sample locations and representative photographs of analyzed samples are  
133 shown in Fig. 2a-b and Fig. 3a-b, respectively.

134 Tourmaline-bearing samples were collected from both veins 1 and 2 (Fig. 3c, e). In hand  
135 specimens, tourmaline grains from both the granite-hosted vein (vein 1) and metasedimentary-  
136 hosted vein (vein 2) are distributed in a matrix of quartz and micas (e.g. biotite and muscovite)  
137 (Fig. 3c, e, h). The abundance of mica in vein 2 is higher than in vein 1 where their occurrence is  
138 limited to halos around tourmaline grains. Within both veins, tourmaline forms local grain  
139 aggregates bound by quartz or overgrowths on disrupted fragments of wall rock enclosed in the  
140 vein quartz (Fig. 3b, c, e). Vein 1 tourmalines form euhedral grains that are greenish-brown under  
141 plane-polarized light, ranging from 0.2 to 1 cm in size, disseminated in clusters within the mineral

142 assemblages of the ore-bearing vein. The metasedimentary-hosted vein 2 tourmalines form  
143 euhedral grains with coloration varying from orange-brown to dark green color and dark blue in  
144 PPL photomicrographs and range from 0.05 to 1 cm in size (Fig. 3f-h). Tourmaline grains from  
145 wall rock sections and quartz-vein hosted tourmaline from granite-hosted vein 1 and  
146 metasedimentary-hosted vein 2 are primarily unzoned. However, some grains show pleochroic hue  
147 and intensity suggesting zonation (Figs. 3d, 4g-h). In BSE images, tourmaline grains from vein 1  
148 and vein 2 show light to dark zonation bands (Fig. 4a). Photomicrographs from vein 2 show higher  
149 occurrence of zoned tourmaline grains in this vein compared to the granite-hosted vein 1 (Fig. 3g-  
150 h). In both quartz-vein and wall rock alteration zones, Fe-Ti oxides, which locally contain Sn,  
151 occur in highly fractured zones within tourmaline (Fig. 3g-h). The unzoned tourmalines are  
152 coexisting or filled with mineral inclusions (e.g. pyrite and zircon) (Fig. 3f, h). Inclusions of these  
153 minerals in unzoned tourmalines are relatively free from fractures suggesting coeval deposition of  
154 sulfides, cassiterite-bearing phases, and tourmaline (Fig. 3h). Albite primarily occurs in wall rock  
155 alteration zones from both vein 1 and 2 suggesting they precipitated during pre-ore metasomatism  
156 (Figs. 3b, 3g, 4b). K-feldspar is partly replaced and co-exists with albite along wall rocks in the  
157 Libata Sn deposit (Fig. 4a). K-feldspar also crystallizes in fractures between tourmaline in granite  
158 wall rock sections from vein 1 in the Libata Sn ore field (Fig. 4b). SEM images show tourmaline-  
159 quartz-chlorite assemblages along ore-bearing structures in the Libata Sn deposit (Fig. 4d-e) with  
160 wall rock samples from vein 1 showing similar alteration assemblage to those in wall rock samples  
161 from vein 2.

## 162 RESULTS

163 Chemical analyses were conducted on tourmalines from the Libata Sn ore field, including  
164 tourmaline major and trace element and B isotope analysis. Additionally, zircon U-Pb dating and

165 Lu-Hf isotopes of zircon from sampled unaltered and altered granites were carried out. Analytical  
166 details related to samples and methods can be found in Online Material<sup>1</sup> while the analytical results  
167 are described below.

### 168 **Zircon morphology and classification**

169 Zircon separated from both the granite porphyry and the altered biotite granite show  
170 variable morphologies and internal textures, as shown by Cathodoluminescence (CL), reflected-,  
171 and transmitted light images (Fig. 6a-c). Zircon grains mostly vary from 50 to 300  $\mu\text{m}$  in diameter,  
172 with length/width ratios between 1:1 and 1:3 (Fig. 6a-b). Three groups of zircons are delineated in  
173 the Libata granites based on morphological and geochemical features: Group 1 zircons are  
174 euhedral to anhedral, showing bright grains with concentric oscillatory zoning (Fig. 6a-b). These  
175 zircon grains exhibit characteristics of magmatic zircons (Table 1). In contrast, Group 2 zircons  
176 are characterized by bright residual cores surrounded by dark, jagged rims, in addition to a few  
177 dark prismatic crystals (Fig. 6a-b). Group 3 zircons exhibit heterogeneous zoning patterns showing  
178 un-zoned areas, rimmed zones with jagged widths/brightness likely reflective of inherited/detrital  
179 zircon grains (Table 1; Fig. 6c). The zircon groups show distinct geochemical signatures based on  
180 zircon discrimination plots proposed by Hoskin (2005). Group 1 zircons largely plot in the field  
181 of magmatic zircons (MZ), while, Group 2 largely plot in the field of hydrothermal zircons and  
182 Group 3 zircon largely plot in the magmatic zircon fields (Fig. 7a-b). Notably, zircon grains that  
183 plot outside the field of magmatic zircons fall within fields of both hydrothermal zircons and  
184 neocrystallized zircons. We interpret the hydrothermal zircon field as representative of original  
185 magmatic zircons that have experienced modification by later hydrothermal fluids to form  
186 hydrothermally altered zircons and the neocrystallized zircon field to represent hydrothermal  
187 zircon grains that precipitated directly from Zr-saturated hydrothermal fluids, respectively (Geisler  
188 et al., 2003; Hoskin, 2005). The zircon grains of the Libata granites are defined by two



189 morphological types, namely a “100” type crystal face that predominantly occurs in the granite  
190 porphyry (sample CR-01) and only sparingly occurs in the altered biotite granite (sample KB-01),  
191 and a “110” type that predominantly occurs in the KB-01 sample with minor amounts in the CR-  
192 01 sample (Fig. 6a-b). The internal textures of zircons vary greatly in back-scattered electron  
193 (BSE), transmitted, and reflected light images. Group 2 zircons from the granite porphyry (CR-01)  
194 and altered biotite granite (KB-01) sample exhibit variable CL characteristics with dark and bright  
195 colors and spongy internal textures (Fig. 6c). The Group 2, mostly “110”-type zircon grains, are  
196 classified as hydrothermally altered zircons (HAZ) based on a combined analysis of zircon CL  
197 images, internal textures, and geochemical characteristics of analyzed zircons in the Libata granite  
198 (Table 1). In summary, eight grains from granite porphyry and seven grains from altered biotite  
199 granites were recognized as HAZ types (Table 1).

## 200 **Zircon U-Pb geochronology**

201 Results of laser ablation inductively coupled plasma mass spectrometry (LA-ICP-MS)  
202 U–Pb dating of zircon grains are listed in Table 2. Low concordance (<90%) zircon grains were  
203 excluded from the above table and concordia plots.

204 Magmatic zircon from the granite porphyry (CR-01) sample yield concordant ages of 650  
205  $\pm 4$  Ma (1 s, mean square of weighted deviate, MSWD = 0.74,  $n=13$ , Fig. 8a), comparable to  
206 weighted-mean  $^{206}\text{Pb}/^{238}\text{U}$  age of  $650 \pm 5$  Ma (1 s, MSWD = 2.80,  $n = 13$ , Fig. 8a). However, a  
207 single grain yields an age of  $421 \pm 5$  Ma, which we interpret as a magmatic grain that has  
208 experienced metamictization and slight Pb-loss (Fig. 6c). In contrast, Group 1 magmatic zircons  
209 from the altered biotite granites (sample KB-01) yield  $^{206}\text{Pb}/^{238}\text{U}$  ages of  $650 \pm 4$  (1 s, MSWD =  
210 1.40,  $n = 12$ ; Fig. 8c), comparable to weighted-mean  $^{206}\text{Pb}/^{238}\text{U}$  age of  $650 \pm 5$  Ma (1 s, MSWD =  
211 1.83,  $n = 12$ , Fig. 8c). Two magmatic zircon grains from the altered biotite granite show  $^{206}\text{Pb}/^{238}\text{U}$

212 ages of  $867 \pm 5$  Ma and  $963 \pm 7$  Ma, respectively. We interpret these ages as inherited zircon ages  
213 from detrital zircons (Fig. 6c).

214 Group 2 HAZ grains from the granite porphyry yield concordant ages of  $650 \pm 6$  Ma (1 s,  
215 MSWD = 0.87,  $n = 7$ , Fig. 8b), comparable to weighted-mean  $^{206}\text{Pb}/^{238}\text{U}$  age of  $650 \pm 8$  Ma (1 s,  
216 MSWD = 2.70,  $n = 7$ , Fig. 8b). Contrastingly, group 2 HAZ grains from the altered biotite granite  
217 yield  $^{206}\text{Pb}/^{238}\text{U}$  concordant ages of  $650 \pm 5$  Ma (1 s, MSWD = 3.20,  $n = 5$ ; Fig. 8d), comparable  
218 to weighted-mean  $^{206}\text{Pb}/^{238}\text{U}$  age of  $650 \pm 5$  Ma (1 s, MSWD = 6.18,  $n = 5$ , Fig. 8d).

### 219 **Zircon trace element compositions**

220 Trace element compositions of zircon from the studied rocks are given in Online Material<sup>2</sup>  
221 Table OM1. Trace element concentrations vary significantly between magmatic and  
222 hydrothermally altered zircon in the unmineralized and altered granites. In the granite porphyry  
223 sample (CR-01), Group 1 (magmatic) zircons are characterized by low P (avg = 340 ppm), Y (avg  
224 = 754 ppm), Hf (avg = 9834 ppm), U (147 ppm), and  $\Sigma\text{REE}$  (avg = 550 ppm). In contrast, Group  
225 2 hydrothermally altered zircons show higher average P (1211 ppm), Y (850 ppm), Hf (9972 ppm),  
226 U (175 ppm), and  $\Sigma\text{REE}$  (698 ppm) values. Compared to magmatic zircon, hydrothermal zircon  
227 from sample CR-01 shows flat HREE with relatively weak positive Eu anomaly ( $\text{Eu}/\text{Eu}^* = 0.05$ –  
228 0.07) and positive Ce anomaly ( $\text{Ce}/\text{Ce}^* = 1.2$ –46.9; Fig. 8e). Trace element and REE distribution  
229 for both magmatic and hydrothermally altered zircons from the altered biotite granites also show  
230 moderate variation trends. HAZ grains in the altered biotite granites are characterized by high  
231 values of Y (467–1351 ppm, average = 776 ppm), Hf (8250–10086 ppm, average = 9325 ppm), P  
232 (443–3632 ppm, average = 1299 ppm), and  $\Sigma\text{REE}$  (428–944 ppm, average = 650 ppm).  
233 Corresponding values from MZ in the altered biotite granites are markedly lower (P = 101–426  
234 ppm, average = 237 ppm; Y = 283–2274 ppm, average = 737 ppm; Hf = 7360–10045 ppm, average

235 = 8844 ppm;  $\Sigma\text{REE} = 235\text{--}1517$  ppm, average = 566 ppm). However, they exhibit negative Eu  
236 anomaly ( $\text{Eu}/\text{Eu}^* = 0.06\text{--}0.54$ ) with weakly positive Ce anomaly ( $\text{Ce}/\text{Ce}^* = 1.3\text{--}2.9$ ; Fig. 8f).

### 237 **Zircon Lu-Hf isotopes**

238 Twenty-four representative zircon spots were selected for Hf isotopic analysis (Table 3).  
239 MZ from the unmineralized granite porphyry (sample CR-01) show a narrow range of  $\epsilon\text{Hf}(t)$  (+4.4  
240 to +5.6),  $^{176}\text{Lu}/^{177}\text{Hf}$  (0.000610–0.000756),  $^{176}\text{Yb}/^{177}\text{Hf}$  (0.025232–0.032046), and variable  
241  $^{176}\text{Hf}/^{177}\text{Hf}$  (0.282494–0.282534) values. On the other hand, HAZ grains from the Libata granite  
242 porphyry show overlapping  $\epsilon\text{Hf}(t)$  (+4.5 to +6.2) and  $^{176}\text{Hf}/^{177}\text{Hf}$  (0.282502–0.282545) but higher  
243  $^{176}\text{Lu}/^{177}\text{Hf}$  (0.000573–0.001012) and  $^{176}\text{Yb}/^{177}\text{Hf}$  (0.023931–0.044225) values. Calculated two-  
244 stage Hf model ages for the granite porphyry show Mesoproterozoic crustal Model ages ( $T_{\text{DM}}^{\text{C}} =$   
245 1311 to 1200 Ma) (Table 3). MZ in the altered biotite granite also show variable Lu-Hf-Yb isotopic  
246 ratios, namely  $^{176}\text{Hf}/^{177}\text{Hf}$  (0.282521–0.282591),  $^{176}\text{Lu}/^{177}\text{Hf}$  (0.000554–0.000927),  $^{176}\text{Yb}/^{177}\text{Hf}$   
247 (0.019038–0.039216), and  $\epsilon\text{Hf}(t)$  values of +5.2 to +7.9. Comparatively, HAZ grains from the  
248 altered biotite granite show higher  $\epsilon\text{Hf}(t)$  (+6.3 to +10.9),  $^{176}\text{Lu}/^{177}\text{Hf}$  (0.000657–0.001227),  
249  $^{176}\text{Yb}/^{177}\text{Hf}$  (0.028083–0.054186) but variable  $^{176}\text{Hf}/^{177}\text{Hf}$  (0.282544–0.282676). Calculated two-  
250 stage Hf model ages for the altered biotite granite show Mesoproterozoic to Neoproterozoic crustal  
251 model ages ( $T_{\text{DM}}^{\text{C}} = 1254$  to 900 Ma) (Table 3). Two crystals (one metamict and one inherited  
252 magmatic) from our samples are characterized by variable  $^{176}\text{Hf}/^{177}\text{Hf}$  ratios (0.281972–0.282529)  
253 and yielding outliers of  $\epsilon\text{Hf}(t)$  (–7.5 to +0.5) and  $T_{\text{DM}}^{\text{C}}$  (1378–2293 Ma). Due to the standard  
254  $f\text{Lu}/\text{Hf}$  values ( $< -0.9$ ), obtained from analyzed zircon grains in this study, calculated Hf  $T_{\text{DM}}^{\text{C}}$   
255 modal ages are considered reliable estimates of crustal residence times (Wang et al., 2016).

### 256 **Tourmaline EPMA data**

257 Tourmalines from the veins 1 and 2 in the Libata Sn ore field exhibit similar major  
258 elemental compositions (Online Material<sup>3</sup> Table OM1). They have variable F (0.03–0.49 wt%),

259 CaO (0.10–1.28 wt%) and MgO (1.85–4.62 wt%), high SiO<sub>2</sub> (34.36–36.48 wt%), Al<sub>2</sub>O<sub>3</sub> (29.93–  
260 33.40 wt%), FeO (11.03–13.95 wt%), and TiO<sub>2</sub> (0.36–1.01 wt%), as well as low MnO (0.15–0.81  
261 wt%). Based on the X-site occupancy and according to the classification of Henry et al. (2011),  
262 the tourmalines from both veins belong to the alkali group (Fig. 9a). The tourmalines display a  
263 large variation in Mg/(Mg + Fe) ratios from 0.2 to 0.4, with all the tourmaline samples showing  
264 schorl compositions (Fig. 9b). The tourmalines also shows high total Al (6.0–6.5 apfu), moderate  
265 excess Al in octahedral Y-sites (up to 0.5 apfu), moderate F contents (up to 0.3 apfu) and variable  
266 X-site vacancy content (0.2 to 0.4 apfu) whereby the Na cation is dominant in the X-site (0.6–0.7;  
267 Online Material<sup>3</sup> Table OM1). The tourmalines from vein 1 and 2 plot in the field of Li-poor  
268 granitoids, pegmatites, and aplites (Fig. 9b) based on discrimination plots of Al-Fe-Mg (Henry and  
269 Guidotti, 1985).

#### 270 **In situ tourmaline trace elements**

271 Trace element compositions of tourmaline from the Libata Sn-W deposit are given in  
272 Online Material<sup>3</sup> Table OM2. Tourmaline is overall characterized by low concentrations (< 0.1–  
273 10 ppm) of Co, Ni, Cu, Rb, Y, REE, Zr, Nb, Mo, Cs, Ba, Ta, W, Pb, Bi, Th, and U, moderate  
274 concentrations (10 s to 100 ppm) of Be, Sc, and Sr, and high concentrations (100s ppm to >1000  
275 ppm) of Li, Sn, Ga, V, and Zn (Online Material<sup>3</sup> Table OM2). Multi-element normalized to average  
276 continental crust values from Rudnick and Gao (2003) (Fig. 9c) show only a few elements reach  
277 concentration levels at or above those of the average crust (Sn, Zn, Li, Ta, V, Co, Ni, and Sc) (Fig.  
278 9c). Chondrite-normalized REE plots (Fig. 9d) overall also show low concentrations and a high  
279 variability of REE distribution from the Libata tourmaline. Overall, the vein 1 tourmalines show  
280 higher total REE values (avg = 11.4 ppm, standard deviation (Stdev): 5) than those from vein 2  
281 (avg = 9.8 ppm, Stdev = 4) (Online Material<sup>3</sup> Table OM2). The tourmalines from veins 1 and 2

282 show a negative sloping pattern from light through middle REE concentrations to a slightly  
283 positive sloping pattern towards the heavy REE segment, and a weakly positive Eu anomaly on  
284 chondrite-normalized REE plots (Fig. 9d).

285 To identify trace element correlations in our dataset, we applied principal component  
286 analysis (PCA), a multivariate statistical technique that provides dimensionality-reduction of  
287 correlated variables into a reduced set of orthogonal linear combinations. This technique is  
288 particularly useful for analyzing large geochemical datasets including LA-ICP-MS trace element  
289 data, maximizing variance, and minimizing information loss (Winderbaum et al., 2012; Harlaux  
290 et al., 2019; Codeço et al., 2021). PCA was applied on log-transformed LA-ICP-MS trace element  
291 data from the Libata tourmaline (n = 49 spots). 15 variables were selected for the PCA including  
292 the main trace elements (Li, Sc, V, Cr, Co, Ni, Zn, Ga, Ge, Sr, Nb, In, Sn, Pb, and Ta). Elements  
293 with very low concentrations (< 1 ppm) or below the limits of detection were excluded. Results of  
294 the two-dimensional projection of the two first principal components (PC1 vs. PC2), showing the  
295 statistical correlations between the investigated variables on a correlation circle is given in Fig. 9e-  
296 f. For the Libata tourmalines, four main groups of element correlation clusters are discriminated  
297 by the PCA. Group 1 comprised of Co, Ga, Ni, Cr, Sc, and In characterizes the higher  
298 concentrations in vein 1 tourmalines (Fig. 9f; Online Material<sup>3</sup> Table OM2). Group 2 composed  
299 of Li and Zn shows the variability of vein 2 tourmalines. Overlapping concentrations in Group 3  
300 and 4 (Nb-Ta and Sc-V) precludes the discrimination of distinct clusters. Some elements (i.e. Sn,  
301 Ge, In, and Pb) plot individually, without correlations between each other. Trace elements show  
302 overlapping concentrations between the core and rim from vein 1 and 2 and therefore preclude the  
303 discrimination of distinct clusters (Online Material<sup>3</sup> Table OM2).

## 304 **Boron isotopes**

305 The LA–MC–ICP–MS boron isotopic data of tourmalines from our study are available in  
306 Online Material<sup>3</sup> Table OM3 and illustrated in Fig. 10. The vein 1-type tourmalines show a narrow  
307 range of  $\delta^{11}\text{B}$  values between  $-15.7 \pm 0.4\text{‰}$  and  $-14.4 \pm 0.5\text{‰}$ , with a weighted mean value of  
308  $-15.0 \pm 0.2\text{‰}$  ( $n = 27$ , MSWD = 0.48) (Fig. 10a). Cores from zoned tourmaline grains from vein  
309 1 show higher  $\delta^{11}\text{B}$  values compared to the rims (Online Material<sup>3</sup> Table OM3). The vein 2  
310 tourmalines show markedly higher  $\delta^{11}\text{B}$  values than the vein 1 type, ranging from  $-15.1 \pm 0.4\text{‰}$   
311 and  $-14.1 \pm 0.3\text{‰}$ , with a weighted mean value of  $-14.6 \pm 0.1\text{‰}$  ( $n = 42$ , MSWD = 0.49) (Fig.  
312 10a). Within sample variations between core and rim in zoned tourmaline from vein 2 are typically  
313  $<1\text{‰}$  (Fig. 4a) with cores showing higher average in  $\delta^{11}\text{B}$  values compared to rims (Online  
314 Material<sup>3</sup> Table OM3).

## 315 **DISCUSSION**

### 316 **Geochemical features of zircons from the Libata Sn-W ore field**

317 To track the degree of alteration between Group 1 and Group 2 zircons in the Libata ore  
318 field, we applied the discrimination indices ( $\text{LREE-I} = \text{Dy/Nd} + \text{Dy/Sm}$ ) proposed by Bell et al.  
319 (2019). Magmatic zircons from the granite porphyry and altered biotite granite display higher  
320 LREE-I values (sample CR-01: 4.3–95.8, average = 56.8,  $n = 15$ ; sample KB-01: 23.9–81.5,  
321 average = 50.1,  $n = 14$ ) than corresponding HAZs (CR01: 3.3–82.6, average = 27.1,  $n = 8$ ; sample  
322 KB-01: 3.7–30.4, average = 21.3,  $n = 7$ ) from the studied samples (Fig. 7c-d). The low LREE-I  
323 values (Online Material<sup>2</sup> Table OM1) in the HAZ grains along with the textural alteration is  
324 indicative of post-magmatic modification from fluid-zircon interactions (Bell et al., 2019).  
325 Generally, trace and minor (Hf, U, Y, Th, LREE, etc.) element concentrations in HAZs are  
326 markedly higher than values in magmatic zircons (Hoskin, 2005; Li et al., 2014). Due to the higher

327 mobility of LREEs relative to HREEs in hydrothermal phases, LREEs are preferentially  
328 incorporated into hydrothermally altered, metamict and hydrothermal zircon grains (Sheard et al.,  
329 2012). In the Libata granites, hydrothermally altered zircons are enriched in LREE and  $\Sigma$ REE  
330 when compared to magmatic zircons (Figs. 7e-f; 8e-f).

331 Titanium-in-zircon thermometry (Ferry and Watson, 2007) has been recognized as a  
332 reliable indicator for zircon crystallization and host magma temperatures (Schiller and Finger,  
333 2019; Vincent et al., 2021). However, the reliability of the Ti-in-zircon temperatures is dependent  
334 on the preservation of Ti concentrations in zircon, which may become perturbed during highly  
335 mobile phases that form HAZ (Fu et al., 2008; Bloch et al., 2022). For the Libata granites, the  
336 application of Ti-in-zircon geothermometry to delineate crystallization temperatures of the  
337 hydrothermal zircon grains is not feasible due to the markedly high Ti concentrations in  
338 neocrystallized and HAZ (Online Material<sup>2</sup> Table OM1). However, the crystallization  
339 temperatures can be derived from zircon morphology due to the large dependence of prism shapes  
340 on crystallization temperatures (Pupin, 1980; Dill et al., 2012). High crystallization temperatures  
341 ( $>800$  °C) favor the growth of “100” type prisms whereas moderate to low temperatures ( $<700$  °C)  
342 favor the development of “110” type prisms (Hayashi and Shinno, 1990). For the Libata granites,  
343 most magmatic zircons show “100” prisms, while hydrothermal zircons generally exhibit “110”  
344 prisms (Fig. 6a-b). Zircon morphology combined with Ti-in-zircon geothermometry from  
345 magmatic zircons in the granite porphyry (avg.  $761 \pm 11$  °C) and altered biotite granites (avg.  $717$   
346  $\pm 12$  °C) samples confirm high initial crystallization temperatures ( $>700$  °C) for the Libata granites.  
347 The dominance of “110” prisms in hydrothermal zircons from the Libata ore field likely reflects  
348 zircon metamictization in these grains. The presence of these “110” prisms also point to a shift  
349 towards late-stage magmatic-hydrothermal conditions since metamict zircons are typically

350 crystallized from highly evolved late residual melt (Kozlik et al., 2016). Their late-stage origin and  
351 typical “110” form suggests relatively low closure temperatures (<650 °C) for the hydrothermal  
352 zircons (Fig. 6a-b) in the Libata granites (Jiang et al., 2019a).

### 353 **Timing of magmatic-hydrothermal activities in the Libata ore field**

354 The zircon U-Pb ages from our study allow for precise timing of magmatic activity in the  
355 Libata Sn deposit and its implication for the magmatic-hydrothermal episodes in the Libata ore  
356 field. Zircon U-Pb ages for Libata granites cluster around ~650 Ma (Table 1). Group 1 magmatic  
357 zircons from the Libata granite porphyry and altered biotite granite yield U–Pb concordant ages of  
358  $650 \pm 4$  (1 s, MSWD = 0.74, n = 13), and  $650 \pm 4$  Ma (1 s, MSWD = 1.40, n = 12), respectively  
359 (Fig. 8a, c). The zircon U-Pb ages from the Libata granites (650 Ma) confirm their emplacement  
360 during the peak of the Pan-African orogenic episode in western Nigerian terrain (Bute et al., 2019;  
361 Ferré et al., 1996). Our zircon U-Pb ages are markedly similar to ages ( $642 \pm 6$  Ma) obtained from  
362 quartz potassic syenites from southwestern Nigeria (Adetunji et al., 2016). They also overlap U-  
363 Pb ages from other Pan-African suites (580-751 Ma) from the eastern and western terrain of the  
364 Nigerian basement (Ferré et al., 1996; Ferré et al., 1998).

365 The utility of LA-ICP-MS U-Pb dating of hydrothermal zircons to constrain timing of  
366 hydrothermal episodes have been demonstrated for Pb-Zn-Cu (Vincent et al., 2021), Au (Bao et  
367 al., 2014), and Sn–W deposits (Jiang et al., 2019a; Jiang et al., 2019b). In the Libata ore field,  
368 Group 2 HAZs in sample CR-01 and Sample KB-01 yield ages of  $650 \pm 6$  Ma (1 s, MSWD = 0.87,  
369 n = 7) and  $650 \pm 5$  Ma (1 s, MSWD = 3.20, n = 5), respectively (Fig. 8b, d). In this study, the  
370 concordant ages from HAZs in both the Libata granite porphyries and altered biotite granite (650  
371 Ma) suggests they were modified immediately after the crystallization of the host granite intrusions.



## 372 **Source of melts and ore-forming materials for the Libata Sn deposit**

373 Trace element and Hf isotope variation are suitable tracers of distinct magma sources and  
374 melt evolutionary history in magmatic rocks (Kemp et al., 2005). Consequently, we apply  
375 discrimination ratios based on magmatic zircon trace element chemistry to constrain source(s) and  
376 evolution of the Libata granitoids. Zircon U/Yb vs. Yb (Fig. 11a) show that samples from the  
377 Libata ore field mostly fall in the continental zircon field and suggest a continental origin for the  
378 Libata granitoids (Grimes et al., 2007). Furthermore, zircon U/Yb vs. Nb/Yb discrimination plots  
379 (Fig. 11b) imply a continental arc-related tectonic regime for the Libata intrusions and suggests  
380 granite emplacement in a continental margin. Applying our zircon Lu-Hf isotope data, the Libata  
381 granites show high positive  $\epsilon_{\text{Hf}}(t)$  (+4.4 to +10.6, average, = +6.4; Table 3) values. These values  
382 are higher than  $\epsilon_{\text{Hf}}(t)$  signatures from inherited zircons in the Libata granites ( $\epsilon_{\text{Hf}}(t) = -7.6$ ) and  
383 other granitoids in the Benino-Nigerian shield within the range of 656–610 Ma yielding negative  
384  $\epsilon_{\text{Hf}}(t)$  (–27.1 to –6.4) (Ganade et al., 2016). Our  $\epsilon_{\text{Hf}}(t)$  values are below depleted mantle values  
385 (Fig. 12a; Table 3) showing positive  $\epsilon_{\text{Hf}}(t)$  values which rule out anataxis of local crustal rocks  
386 and reflective of source rocks derived from a mantle source. Calculated Hf model ages for the  
387 Libata granites (0.8–1.3 Ga) are lower than the values from other 656–610 Ma granites from the  
388 Benino-Nigerian shield (1.5–3.4 Ga) suggesting, limited contamination of the primary mantle  
389 melts with crustal material.

390 Lu–Hf isotopic compositions of hydrothermal zircons are distinct from signatures in  
391 magmatic zircons and provide a viable tool for tracking fluid sources and evolutionary processes  
392 in magmatic-hydrothermal systems (Li et al., 2018). The  $^{176}\text{Hf}/^{177}\text{Hf}$  ratios are similar in the  
393 magmatic and hydrothermally altered zircons from the Libata granitoids (Table 3), indicating the  
394 preservation of the Hf isotopic system in zircon (Lenting et al., 2010). However,  $^{176}\text{Lu}/^{177}\text{Hf}$  (up  
395 to 0.0012) and  $^{176}\text{Yb}/^{177}\text{Hf}$  (up to 0.055) ratios are markedly higher in HAZ compared to MZ from

396 the Libata granites (Fig. 12c-d) explained by higher mobility of Lu and Yb during hydrothermal  
397 phases associated with zircon alteration (Lenting et al., 2010). The similar and broadly overlapping  
398  $\epsilon_{\text{Hf}}(t)$  values for magmatic and hydrothermally altered zircon grains from the Libata orefield  
399 (Table 3) suggest that the mineralizing fluids were likely sourced from the granitic magmas.

400 The  $\delta^{11}\text{B}$  values in tourmaline from the ore bearing veins in the Libata Sn ore field range  
401 from  $-15.7\text{‰}$  to  $-14.7\text{‰}$  (Fig. 10a-b). Vein 1 tourmalines have  $\delta^{11}\text{B}$  values of  $-15.7$  to  $-14.4\text{‰}$   
402 (average =  $-15.0\text{‰}$ ), whilst vein 2 tourmalines show  $\delta^{11}\text{B}$  values of  $-15.1$  to  $-14.1\text{‰}$  (average =  
403  $-14.6\text{‰}$ ). Due to limited fluid inclusion data from the Libata Sn deposit, we infer temperature  
404 conditions of the primary hydrothermal fluids to derive fluid-tourmaline equilibrium temperatures.  
405 Assuming crystallization temperatures of 400 to 500 °C, equilibrium fluid-tourmaline fractionation  
406 at 500 °C and 400 °C are  $+1.9\text{‰}$  and  $+2.7\text{‰}$ , respectively (Meyer et al., 2008). This suggests that  
407 the  $\delta^{11}\text{B}$  values of the fluids in isotopic equilibrium were  $-13.1$  to  $-12.3\text{‰}$  for the vein 1  
408 tourmalines and  $-12.7$  to  $-11.9\text{‰}$  for the vein 2 tourmalines. The emplacement of vein 1 firmly  
409 within the Libata granites suggests derivation of boron predominantly from magmatic fluids  
410 exsolved from granitic melts. To test for a granitic fluid source, we estimate the isotopic  
411 compositions of a granitic melt that produces a magmatic fluid with a  $\delta^{11}\text{B}$  of  $-12.3$  to  $-13.1\text{‰}$   
412 for the granite-hosted vein 1. At temperatures of 650 °C estimated for the hydrous F-rich granitic  
413 melt and assuming 50:50 proportion of trigonal-tetrahedral coordination of boron in the melt  
414 (Trumbull et al., 2013), a B-isotope fractionation factors of  $5\text{‰}$  between granitic melt and fluid is  
415 calculated from molecular dynamics (Kowalski et al., 2013). This would imply  $\delta^{11}\text{B}$  values of  
416  $-17.3$  to  $-18.1\text{‰}$  for the hypothetical granitic source, which falls in the range of values from  
417 granites (Trumbull et al., 2020). For the metasedimentary-hosted vein 2, the markedly similar trace  
418 element (Fig. 9a-d) and close overlap in boron isotopic values (Fig. 10b) with tourmalines from

419 the granite-hosted vein 1 suggests ore materials/fluids in vein 2 were sourced from either the same  
420 source as the granite-hosted vein 1 or from shallow magmatic bodies. The difference between  $\delta^{11}\text{B}$   
421 compositions from veins 1 and 2 (Fig. 10a) may reflect differential temperature change between  
422 both veins at constant fluid composition, differing  $\delta^{11}\text{B}$  compositions for zoned rims and cores  
423 from vein 2 or depletion in  $\delta^{11}\text{B}$  during vein fluid vs. wall rock interaction in vein 2.

424 To investigate fluid sources for Sn mineralization in the Libata ore field, we used major  
425 and trace element ratios in tourmaline to track source compositions for the hydrothermal fluids  
426 that precipitated the Libata tourmalines. The Li/Sr ratio provides a good separator for delineating  
427 tourmaline from magmatic vs metamorphic fluid origin (Harlaux et al., 2020). Compared to other  
428 tourmalines hosted in granite and metamorphic rocks (e.g. amphibolites and granite gneiss),  
429 tourmalines from the Libata ore field fall in the compositional field of magmatic tourmaline based  
430 on Li/Sr discrimination plots (Fig. 13a-b) and are in agreement with tourmaline major element  
431 compositions that fall into the field of Li-poor granitoids in the Ca-Fe-Mg diagram (Fig. 8b). The  
432 composition of the Fe-rich schorls from the Libata Sn ore field are in agreement with tourmaline  
433 compositions from most granitic rocks and magmatic-hydrothermal environments (Pirajno and  
434 Smithies, 1992). Our results are chemically distinct from the schorl-dravite tourmalines from the  
435 Bin-Yauri gold deposit whose origin has been proposed to be from metasedimentary sources  
436 (Garba, 1996). This would suggest that the tourmaline from the Libata Sn veins largely formed  
437 from magmatic fluids. Accordingly, our data suggests derivation of boron in the Libata ore field  
438 was dominantly from magmatic fluids although we do not rule out some contribution from the  
439 metasedimentary rocks in the area.

#### 440 **Magmatic-hydrothermal evolution in the Libata Sn mineralizations**

441 The utility of HAZs as tracers of the nature and chemical compositions of hydrothermal  
442 fluids associated with ore deposits have been widely recognized (Kozlik et al., 2016; Jiang et al.,

443 2019b; Vincent et al., 2021). Experimental studies and natural observations have highlighted the  
444 increased mobility of incompatible elements such as Hf, Th, U, Nb, Ta, Y, P, Sn and Pb in the  
445 presence of volatiles (e.g. B, F, Cl, and H<sub>2</sub>O) (Bau, 1996; Jiang et al., 2020). These highly mobile  
446 fluid-vapor phases are important in alkali-rich granitic systems (Girei et al., 2019; Girei et al., 2020;  
447 Vincent et al., 2021) as well as in B-rich hydrothermal systems (Lehmann, 2020). The high F  
448 concentrations in tourmaline (up to 0.5 wt.%, determined with EPMA) suggest the late-stage  
449 volatile-rich fluids exsolved from the Libata granites were able to carry incompatible elements and  
450 exchange them with Si and Zr from magmatic and metamict zircons through diffusion-controlled  
451 alteration processes that formed HAZs in the Libata granites. Therefore, the hydrothermal fluids  
452 that interacted with these zircons were likely highly enriched in U, Th, F, Y, REE, Nb, Ta, Hf, Fe,  
453 and Ca and moderately enriched in P, Sn, Sc, Pb, and Ti. The Libata HAZs show coupled  
454 correlation trends between U + Nb + Ta and Y +  $\sum$ REE (Fig. 14a) suggesting that many trace  
455 elements have been incorporated into these zircons. Th/U ratios of HAZ in the Libata granites vary  
456 between 0.4 and 0.7 (average = 0.5) and are markedly lower than those of MZ (Fig. 14b). The shift  
457 in Th/U values from magmatic to HAZ is typical for ore deposits and a crucial marker for  
458 delineating hydrothermal zircons (Li et al., 2014). To further track magmatic to hydrothermal  
459 trends in the zircons from the Libata granites, we assessed geochemical ratios (e.g. Y/Ho and  
460 Yb/Gd) that show stable behaviors in primary or anhydrous melts but vary in evolved melts that  
461 are enriched in volatiles and halogens. Other studies have highlighted the stability of Y/Ho in  
462 primary melts where they retain ratios close to chondritic values (Bau, 1996). However, these  
463 ratios show large variations in evolved granitic systems due to increased mobility and behavior of  
464 Y, Zr, Hf, and REEs during volatile-driven mobility (Bau, 1996). HAZ from our studied samples  
465 mostly show elevated Y/Ho values (>28; Fig. 14c) due to complexation with halogen-rich phases

466 with a negative correlation between Y content and Y/Ho ratio present for the magmatic zircon  
467 grains (Jiang et al., 2019a). Differentiation trends for the Libata granites are also traced by Yb/Gd  
468 against Eu/Eu\* values (Fig. 14d). Progressive oxidization conditions along with increased  
469 fractionation during magmatic evolution suggests that the altered biotite granites are more evolved  
470 than the granite porphyries of the Libata ore field (Lu et al., 2019). Furthermore, this trend also  
471 differentiates barren from fertile granite suites with the altered biotite granites largely plotting  
472 above the field synonymous with mineralized granites (Fig. 14d).

473         Geochemical (major and trace element) composition of tourmaline have been widely  
474 recognized as reliable monitor of formation environment and conditions (Dutrow and Henry, 2011).  
475 Moreover, these geochemical signatures have been used extensively to trace evolution in  
476 magmatic-hydrothermal systems (Jiang et al., 2004; Yang et al., 2015; Codeço et al., 2020;  
477 Harlaux et al., 2020). Compositions of tourmalines from Libata, plotting mostly in the schorl field  
478 (Fig. 9b), with low Na contents (average 0.6 apfu) and high X-site vacancies (average 0.3 apfu),  
479 suggesting precipitation from a low-salinity fluid (von Goerne et al., 2001; von Goerne et al., 2011).  
480 Assuming a temperature of 500 °C, a salinity of ca. 3 wt% NaCl eq is estimated for the fluid in  
481 equilibrium with the assemblage tourmaline + quartz + chlorite (von Goerne et al., 2001). REE  
482 patterns of tourmaline generally reflect both the REE composition of the host rock or source as  
483 well as the effects of fluid-rock interactions (Yang et al., 2015; Duchoslav et al., 2017; Hong et al.,  
484 2017). Tourmalines from the Libata ore field show higher concentrations of LREEs relative to  
485 HREEs (Fig. 9d) similar to trends seen in tourmalines from other magmatic-hydrothermal ore  
486 systems (Marks et al., 2013; Yang et al., 2015). This enrichment trend matches REE patterns in  
487 hydrothermal zircons in the Libata granites (Fig. 8e-f) suggesting that the volatile-rich late-stage  
488 fluids responsible for the precipitation of the hydrothermal zircon and tourmaline in the Libata

489 orefield were enriched in LREEs relative to HREEs. Tourmaline from both ore-bearing veins in  
490 the Libata ore field have relatively high Sn (>100 ppm avg) contents (Fig. 13c-d). A coupled  
491 increase in Fe and Sn contents have been reported from tourmalines associated with cassiterite  
492 mineralization (Harlaux et al., 2020). In both veins 1 and 2, the high contents of Fe (13 wt % avg)  
493 and Sn (100 ppm avg.) are notable (Online Material<sup>3</sup> Table OM1 and Online Material<sup>3</sup> Table OM2).  
494 These high concentrations suggest that hydrothermal fluids precipitating tourmaline in the Libata  
495 ore field were rich in Fe and Sn primarily transported as chloride complexes under moderate to  
496 high temperature phases (Taylor and Wall, 1993; Schmidt, 2018). In granitic rocks, mica group  
497 minerals (e.g., biotite) are important hosts of Sn with concentrations ranging from 10s to 100s  
498 parts per million (López-Moro et al., 2017). Mineralizing fluids in Sn ore systems may become  
499 enriched in tin through the breakdown of biotite during chloritization processes (Harlaux et al.,  
500 2020). Elevated vanadium concentrations and the high V/Sc ratios suggest that the hydrothermal  
501 fluid precipitating the tourmalines was rich in vanadium. This enrichment is likely linked to metal  
502 release during biotite chloritization, as biotite is a major host of vanadium (Viswanathan et al.,  
503 2012). Therefore, biotite alteration seen in the Libata granites (Fig. 4c-d) due to chloritization  
504 likely triggered the coupled release of tin and vanadium into the mineralizing fluids, which then  
505 substituted into the crystal lattice of tourmaline during precipitation of hydrothermal tourmalines  
506 in the Libata orefield. Experimental and thermodynamic data support the transport of high  
507 concentrations of tin (100s to 1000s) likely as  $\text{Sn}^{4+}\text{-Cl}$  complexes in hydrothermal fluids (Heinrich,  
508 1990; Schmidt, 2018).

509 Due to their robust ability to retain geochemical signatures from several petrogenetic  
510 processes, tourmaline has been found to be a potential pathfinder mineral for tin deposits (Fogliata  
511 et al., 2012). Elevated trace element concentrations (typically >10s to 100s ppm) of Li, V, Ga, Zn,

512 and Sn in tourmaline grains from the Libata ore field are typical for tourmaline from granite-related  
513 tin deposits (Duchoslav et al., 2017; Codeço et al., 2021). Our data suggests that the high Sn, Zn,  
514 and Li concentration in tourmaline from the Libata ore field can be regarded as ‘indicators’ of  
515 cassiterite mineralization. Accordingly, tracer signatures from tourmaline + chlorite + quartz  
516 alteration assemblages associated with cassiterite-wolframite-niobium mineralization in the Pan-  
517 African granites may serve as valuable indicators for other granite-associated vein-type deposits  
518 in adjacent areas.

## 519 **IMPLICATIONS FOR ORE GENESIS**

520 (1) Our study constrains overlapping magmatic (~650 Ma) and magmatic-hydrothermal  
521 (~650 Ma) events from the Libata granite porphyry and altered biotite granite porphyry. Our ages  
522 are consistent with magmatic-mineralogenic events at the peak of the Pan African orogeny and  
523 expands the known temporal range of granite-related Sn mineralization in the basement complex  
524 of Nigeria.

525 (2) The abundance of metamict and hydrothermally-altered zircons hosted in the granites  
526 adjoining Libata vein 1 and their components suggests that the hydrothermal fluids derived from  
527 the granites likely contributed the ore forming fluids associated with Sn mineralization. The fluids  
528 were enriched in volatile phases (F, Cl, and H<sub>2</sub>O) as well as numerous trace elements such as U,  
529 Y, Nb, Ta, Hf, P, and Ti.

530 (3) Trace element chemistry and B isotopes from both the granite- and metasedimentary-  
531 hosted Sn-Tur veins suggests a common source for ore metals, boron and hydrothermal fluids  
532 forming both veins. Our data point to magmatic-hydrothermal fluids derived from the Libata  
533 granites as the source for ore materials forming the Libata deposit.

534 **ACKNOWLEDGEMENTS**

535

536 We are grateful to Biao Liu and Yuanlin Chen for their help with lab work.

537 **FUNDERS**

538

539 This work was financed by the National Natural Science Foundation of China granted to Dr

540 Huan Li (Grant No. 92162103)

541 **REFERENCES CITED**

542

543 Adetunji, A., Olarewaju, V., Ocan, O., Ganey, V., Macheva, L., 2016. Geochemistry and U-Pb

544 zircon geochronology of the pegmatites in Ede area, southwestern Nigeria: A newly

545 discovered oldest Pan African rock in southwestern Nigeria. *Journal of African Earth*

546 *Sciences*, 115: 177-190.

547 Bao, Z., Sun, W., Li, C., Zhao, Z., 2014. U–Pb dating of hydrothermal zircon from the Dongping

548 gold deposit in North China: constraints on the mineralization processes. *Ore Geology*

549 *Reviews*, 61: 107-119.

550 Bau, M., 1996. Controls on the fractionation of isovalent trace elements in magmatic and aqueous

551 systems: evidence from Y/Ho, Zr/Hf, and lanthanide tetrad effect. *Contributions to*

552 *Mineralogy and Petrology*, 123(3): 323-333.

553 Bell, E.A., Boehnke, P., Barboni, M., Harrison, T.M., 2019. Tracking chemical alteration in

554 magmatic zircon using rare earth element abundances. *Chemical Geology*, 510: 56-71.

555 Bloch, E.M., Jollands, M.C., Tollan, P., Plane, F., Bouvier, A.-S., Hervig, R., Berry, A.J.,

556 Zaubitzer, C., Escrig, S., Müntener, O., 2022. Diffusion anisotropy of Ti in zircon and



- 557 implications for Ti-in-zircon thermometry. *Earth and Planetary Science Letters*, 578:  
558 117317.
- 559 Bute, S.I., Yang, X., Cao, J., Liu, L., Deng, J., Haruna, I.V., Girei, M.B., Abubakar, U., Akhtar,  
560 S., 2019. Origin and tectonic implications of ferroan alkali-calcific granitoids from the  
561 Hawal Massif, east-eastern Nigeria terrane: clues from geochemistry and zircon U-Pb-Hf  
562 isotopes. *International Geology Review*, 62(2): 129-152.
- 563 Cahen, L., Snelling, N., Delhal, J., Vail, J., Bonhomme, M., Ledent, D., 1984. The geochronology  
564 and evolution of Africa. Oxford University Press.
- 565 Claiborne, L.L., Miller, C.F., Wooden, J.L., 2010. Trace element composition of igneous zircon:  
566 a thermal and compositional record of the accumulation and evolution of a large silicic  
567 batholith, Spirit Mountain, Nevada. *Contributions to Mineralogy and Petrology*, 160(4):  
568 511-531.
- 569 Codeço, M.S., Weis, P., Trumbull, R.B., Pinto, F., Lecumberri-Sanchez, P., Wilke, F.D., 2017.  
570 Chemical and boron isotopic composition of hydrothermal tourmaline from the  
571 Panasqueira W-Sn-Cu deposit, Portugal. *Chemical Geology*, 468: 1-16.
- 572 Codeço, M.S., Weis, P., Trumbull, R.B., Van Hinsberg, V., Pinto, F., Lecumberri-Sanchez, P.,  
573 Schleicher, A.M., 2020. The imprint of hydrothermal fluids on trace-element contents in  
574 white mica and tourmaline from the Panasqueira W–Sn–Cu deposit, Portugal. *Mineralium*  
575 *Deposita*, 56: 481-508.
- 576 Codeço, M.S., Weis, P., Trumbull, R.B., Van Hinsberg, V., Pinto, F., Lecumberri-Sanchez, P.,  
577 Schleicher, A.M., 2021. The imprint of hydrothermal fluids on trace-element contents in  
578 white mica and tourmaline from the Panasqueira W–Sn–Cu deposit, Portugal. *Mineralium*  
579 *Deposita*, 56: 481-508.

- 580 Danbatta, U., Garba, M., 2007. Geochemistry and petrogenesis of Precambrian amphibolites in the  
581 Zuru schist belt, northwestern Nigeria. *Journal of Mining and Geology*, 43(1): 23-30.
- 582 Dickin, A., Halliday, A., Bowden, P., 1991. A Pb, Sr and Nd isotope study of the basement and  
583 Mesozoic ring complexes of the Jos Plateau, Nigeria. *Chemical Geology*, 94(1): 23-32.
- 584 Dill, H.G., Weber, B., Klosa, D., 2012. Morphology and mineral chemistry of monazite–zircon-  
585 bearing stream sediments of continental placer deposits (SE Germany): Ore guide and  
586 provenance marker. *Journal of Geochemical Exploration*, 112: 322-346.
- 587 Duchoslav, M., Marks, M.A., Drost, K., McCammon, C., Marschall, H., Wenzel, T., Markl, G.,  
588 2017. Changes in tourmaline composition during magmatic and hydrothermal processes  
589 leading to tin-ore deposition: the Cornubian Batholith, SW England. *Ore Geology Reviews*,  
590 83: 215-234.
- 591 Dutrow, B.L., Henry, D.J., 2011. Tourmaline: a geologic DVD. *Elements*, 7(5): 301-306.
- 592 Ero, K.A., Ekwueme, B.N., 2009. Mineralization of pegmatites in parts of the Oban Massif,  
593 Southeastern Nigeria: A preliminary analysis. *Chinese Journal of Geochemistry*, 28(2):  
594 146-153.
- 595 Ferré, E., Caby, R., Peucat, J., Capdevila, R., Monié, P., 1998. Pan-African, post-collisional, ferro-  
596 potassic granite and quartz–monzonite plutons of Eastern Nigeria. *Lithos*, 45(1-4): 255-  
597 279.
- 598 Ferré, E., Délérís, J., Bouchez, J.-L., Lar, A., Peucat, J.-J., 1996. The Pan-African reactivation of  
599 Eburnean and Archaean provinces in Nigeria: structural and isotopic data. *Journal of the*  
600 *Geological Society*, 153(5): 719-728.

- 601 Ferry, J., Watson, E., 2007. New thermodynamic models and revised calibrations for the Ti-in-  
602 zircon and Zr-in-rutile thermometers. *Contributions to Mineralogy and Petrology*, 154(4):  
603 429-437.
- 604 Fogliata, A.S., Báez, M.A., Hagemann, S., Santos, J., Sardi, F., 2012. Post-orogenic, carboniferous  
605 granite-hosted Sn–W mineralization in the Sierras Pampeanas Orogen, Northwestern  
606 Argentina. *Ore Geology Reviews*, 45: 16-32.
- 607 Fu, B., Page, F.Z., Cavosie, A.J., Fournelle, J., Kita, N.T., Lackey, J.S., Wilde, S.A., Valley, J.W.,  
608 2008. Ti-in-zircon thermometry: applications and limitations. *Contributions to Mineralogy  
609 and Petrology*, 156(2): 197-215.
- 610 Ganade, C.E., Cordani, U.G., Agbossoumounde, Y., Caby, R., Basei, M.A., Weinberg, R.F., Sato,  
611 K., 2016. Tightening-up NE Brazil and NW Africa connections: New U–Pb/Lu–Hf zircon  
612 data of a complete plate tectonic cycle in the Dahomey belt of the West Gondwana Orogen  
613 in Togo and Benin. *Precambrian Research*, 276: 24-42.
- 614 Ganade, C.E., Cordani, U.G., Weinberg, R.F., Basei, M.A., Armstrong, R., Sato, K., 2014. Tracing  
615 Neoproterozoic subduction in the Borborema Province (NE-Brazil): Clues from U-Pb  
616 geochronology and Sr-Nd-Hf-O isotopes on granitoids and migmatites. *Lithos*, 202: 167-  
617 189.
- 618 Garba, I., 1996. Tourmalinization related to Late Proterozoic-Early Palaeozoic lode gold  
619 mineralization in the Bin Yauri area, Nigeria. *Mineralium Deposita*, 31(3): 201-209.
- 620 Garba, I., 2000. Origin of Pan-African mesothermal gold mineralisation at Bin Yauri, Nigeria.  
621 *Journal of African Earth Sciences*, 31(2): 433-449.

- 622 Garba, I., 2003. Geochemical discrimination of newly discovered rare-metal bearing and barren  
623 pegmatites in the Pan-African (600±150 Ma) basement of northern Nigeria. Applied Earth  
624 Science, 112(3): 287-292.
- 625 Geisler, T., Rashwan, A., Rahn, M., Poller, U., Zwingmann, H., Pidgeon, R., Schleicher, H.,  
626 Tomaschek, F., 2003. Low-temperature hydrothermal alteration of natural metamict  
627 zircons from the Eastern Desert, Egypt. Mineralogical Magazine, 67(3): 485-508.
- 628 Girei, M.B., Li, H., Algeo, T.J., Bonin, B., Ogunleye, P.O., Bute, S.I., Ahmed, H.A., 2019.  
629 Petrogenesis of A-type granites associated with Sn–Nb–Zn mineralization in Ririwai  
630 complex, north-Central Nigeria: Constraints from whole-rock SmNd and zircon LuHf  
631 isotope systematics. Lithos, 340: 49-70.
- 632 Girei, M.B., Li, H., Vincent, V.I., Algeo, T.J., Elatikpo, S.M., Bute, S.I., Ahmed, H.A., Amuda,  
633 A.K., 2020. Genesis and timing of Mo mineralization in the Mada Ring Complex, north-  
634 central Nigeria: insights from whole-rock geochemistry, Nd-Sr isotopes, zircon U-Pb-Hf  
635 isotopes, and molybdenite Re-Os systematics. Mineralium Deposita: 1-20.
- 636 Grimes, C., Wooden, J., Cheadle, M., John, B., 2015. “Fingerprinting” tectono-magmatic  
637 provenance using trace elements in igneous zircon. Contributions to Mineralogy and  
638 Petrology, 170(5-6): 46.
- 639 Grimes, C.B., John, B.E., Kelemen, P., Mazdab, F., Wooden, J., Cheadle, M.J., Hanghøj, K.,  
640 Schwartz, J., 2007. Trace element chemistry of zircons from oceanic crust: A method for  
641 distinguishing detrital zircon provenance. Geology, 35(7): 643-646.
- 642 Harlaux, M., Kouzmanov, K., Gialli, S., Laurent, O., Rielli, A., Dini, A., Chauvet, A., Menzies,  
643 A., Kalinaj, M., Fontboté, L., 2020. Tourmaline as a tracer of late-magmatic to

- 644 hydrothermal fluid evolution: the world-class San Rafael tin (-copper) deposit, Peru.  
645 Economic Geology, 115(8): 1665-1697.
- 646 Harlaux, M., Mercadier, J., Marignac, C., Villeneuve, J., Mouthier, B., Cuney, M., 2019. Origin  
647 of the atypical Puy-les-Vignes W breccia pipe (Massif Central, France) constrained by  
648 trace element and boron isotopic composition of tourmaline. Ore Geology Reviews, 114:  
649 103132.
- 650 Hayashi, M., Shinno, I., 1990. Morphology of synthetic zircon crystals doped with various  
651 elements. Mineralogical Journal, 15(3): 119-128.
- 652 Hazarika, P., Mishra, B., Pruseth, K.L., 2015. Diverse tourmaline compositions from orogenic  
653 gold deposits in the Hutti-Maski greenstone belt, India: implications for sources of ore-  
654 forming fluids. Economic Geology, 110(2): 337-353.
- 655 Heinrich, C.A., 1990. The chemistry of hydrothermal tin (-tungsten) ore deposition. Economic  
656 Geology, 85(3): 457-481.
- 657 Henry, D.J., Guidotti, C.V., 1985. Tourmaline as a petrogenetic indicator mineral: an example  
658 from the staurolite-grade metapelites of NW Maine. American mineralogist, 70(1-2): 1-15.
- 659 Henry, D.J., Novák, M., Hawthorne, F.C., Ertl, A., Dutrow, B.L., Uher, P., Pezzotta, F., 2011.  
660 Nomenclature of the tourmaline-supergroup minerals. American Mineralogist, 96(5-6):  
661 895-913.
- 662 Hong, W., Cooke, D.R., Zhang, L., Fox, N., Thompson, J., 2017. Tourmaline-rich features in the  
663 Heemskirk and Pieman Heads granites from western Tasmania, Australia: Characteristics,  
664 origins, and implications for tin mineralization. American Mineralogist, 102(4): 876-899.

- 665 Hoskin, P.W., 2005. Trace-element composition of hydrothermal zircon and the alteration of  
666 Hadean zircon from the Jack Hills, Australia. *Geochimica et Cosmochimica Acta*, 69(3):  
667 637-648.
- 668 Jiang, S.-Y., Yu, J.-M., Lu, J.-J., 2004. Trace and rare-earth element geochemistry in tourmaline  
669 and cassiterite from the Yunlong tin deposit, Yunnan, China: implication for migmatitic–  
670 hydrothermal fluid evolution and ore genesis. *Chemical Geology*, 209(3-4): 193-213.
- 671 Jiang, W.-C., Li, H., Evans, N.J., Wu, J.-H., 2019a. Zircon records multiple magmatic-  
672 hydrothermal processes at the giant Shizhuyuan W–Sn–Mo–Bi polymetallic deposit, South  
673 China. *Ore Geology Reviews*, 115: 103160.
- 674 Jiang, W.-C., Li, H., Mathur, R., Wu, J.-H., 2019b. Genesis of the giant Shizhuyuan W–Sn–Mo–  
675 Bi–Pb–Zn polymetallic deposit, South China: Constraints from zircon geochronology and  
676 geochemistry in skarns. *Ore Geology Reviews*, 111(1): 102980.
- 677 Jiang, W.-C., Li, H., Turner, S., Zhu, D.-P., Wang, C., 2020. Timing and origin of multi-stage  
678 magmatism and related W–Mo–Pb–Zn–Fe–Cu mineralization in the Huangshaping deposit,  
679 South China: An integrated zircon study. *Chemical Geology*, 552: 119782.
- 680 Kemp, A., Wormald, R., Whitehouse, M., Price, R., 2005. Hf isotopes in zircon reveal contrasting  
681 sources and crystallization histories for alkaline to peralkaline granites of Temora,  
682 southeastern Australia. *Geology*, 33(10): 797-800.
- 683 Kinnaird, J., Bowden, P., 1987. African anorogenic alkaline magmatism and mineralization—a  
684 discussion with reference to the Niger-Nigerian Province. *Geological Journal*, 22(S2): 297-  
685 340.
- 686 Kinnaird, J.A., Nex, P.A., Milani, L., 2016. Tin in Africa. *Episodes*, 39(2): 361-380.

- 687 Kowalski, P.M., Wunder, B., Jahn, S., 2013. Ab initio prediction of equilibrium boron isotope  
688 fractionation between minerals and aqueous fluids at high P and T. *Geochimica et*  
689 *Cosmochimica Acta*, 101: 285-301.
- 690 Kozlik, M., Raith, J.G., Gerdes, A., 2016. U–Pb, Lu–Hf and trace element characteristics of zircon  
691 from the Felbertal scheelite deposit (Austria): New constraints on timing and source of W  
692 mineralization. *Chemical Geology*, 421: 112-126.
- 693 Lehmann, B., 2020. Formation of tin ore deposits: A reassessment. *Lithos*: 105756.
- 694 Lenting, C., Geisler, T., Gerdes, A., Kooijman, E., Scherer, E.E., Zeh, A., 2010. The behavior of  
695 the Hf isotope system in radiation-damaged zircon during experimental hydrothermal  
696 alteration. *American Mineralogist*, 95(8-9): 1343-1348.
- 697 Li, H., Watanabe, K., Yonezu, K., 2014. Zircon morphology, geochronology and trace element  
698 geochemistry of the granites from the Huangshaping polymetallic deposit, South China:  
699 Implications for the magmatic evolution and mineralization processes. *Ore Geology*  
700 *Reviews*, 60: 14-35.
- 701 Li, H., Wu, J.-H., Evans, N.J., Jiang, W.-C., Zhou, Z.-K., 2018. Zircon geochronology and  
702 geochemistry of the Xianghualing A-type granitic rocks: Insights into multi-stage Sn-  
703 polymetallic mineralization in South China. *Lithos*, 312: 1-20.
- 704 López-Moro, F.J., Polonio, F.G., González, T.L., Contreras, J.L.S., Fernández, A.F., Benito,  
705 M.C.M., 2017. Ta and Sn concentration by muscovite fractionation and degassing in a lens-  
706 like granite body: The case study of the Penouta rare-metal albite granite (NW Spain). *Ore*  
707 *Geology Reviews*, 82: 10-30.

- 708 Lu, Y., Smithies, R.H., Wingate, M., Evans, N., McCuaig, T., Champion, D., Outhwaite, M., 2019.  
709 Zircon fingerprinting of magmatic-hydrothermal systems in the Archean Yilgarn craton.  
710 Perth: Geological Survey of Western Australia, 22.
- 711 Ludwig, T., Marschall, H., von Strandmann, P.P., Shabaga, B., Fayek, M., Hawthorne, F., 2011.  
712 A secondary ion mass spectrometry (SIMS) re-evaluation of B and Li isotopic  
713 compositions of Cu-bearing elbaite from three global localities. Mineralogical Magazine,  
714 75(4): 2485-2494.
- 715 Marks, M.A., Marschall, H.R., Schühle, P., Guth, A., Wenzel, T., Jacob, D.E., Barth, M., Markl,  
716 G., 2013. Trace element systematics of tourmaline in pegmatitic and hydrothermal systems  
717 from the Variscan Schwarzwald (Germany): The importance of major element composition,  
718 sector zoning, and fluid or melt composition. Chemical Geology, 344: 73-90.
- 719 Marschall, H.R., Jiang, S.-Y., 2011. Tourmaline isotopes: no element left behind. Elements, 7(5):  
720 313-319.
- 721 McCurry, P., 1971. Pan-African orogeny in northern Nigeria. Geological Society of America  
722 Bulletin, 82(11): 3251-3262.
- 723 Melcher, F., Graupner, T., Gäbler, H.-E., Sitnikova, M., Henjes-Kunst, F., Oberthür, T., Gerdes,  
724 A., Dewaele, S., 2015. Tantalum–(niobium–tin) mineralisation in African pegmatites and  
725 rare metal granites: constraints from Ta–Nb oxide mineralogy, geochemistry and U–Pb  
726 geochronology. Ore Geology Reviews, 64: 667-719.
- 727 Meyer, C., Wunder, B., Meixner, A., Romer, R.L., Heinrich, W., 2008. Boron-isotope  
728 fractionation between tourmaline and fluid: an experimental re-investigation.  
729 Contributions to Mineralogy and Petrology, 156(2): 259-267.



- 730 Okunlola, O.A., Ocan, O.O., 2009. Rare metal (Ta-Sn-Li-Be) distribution in Precambrian  
731 pegmatites of Keffi area, Central Nigeria. *Nature and Science*, 7: 90-99.
- 732 Olade, M.A., 2021. *Mineral Deposits and Exploration Potential of Nigeria*. Prescott books.
- 733 Petersson, A., Scherstén, A., Gerdes, A., 2018. Extensive reworking of Archaean crust within the  
734 Birimian terrane in Ghana as revealed by combined zircon U-Pb and Lu-Hf isotopes.  
735 *Geoscience Frontiers*, 9(1): 173-189.
- 736 Pirajno, F., Smithies, R., 1992. The FeO/(FeO+ MgO) ratio of tourmaline: a useful indicator of  
737 spatial variations in granite-related hydrothermal mineral deposits. *Journal of Geochemical*  
738 *Exploration*, 42(2-3): 371-381.
- 739 Pupin, J., 1980. Zircon and granite petrology. *Contributions to Mineralogy and Petrology*, 73(3):  
740 207-220.
- 741 Rudnick, R., Gao, S., 2003. Composition of the continental crust. *The crust*, 3: 1-64.
- 742 Schiller, D., Finger, F., 2019. Application of Ti-in-zircon thermometry to granite studies: problems  
743 and possible solutions. *Contributions to Mineralogy and Petrology*, 174(6): 51.
- 744 Schmidt, C., 2018. Formation of hydrothermal tin deposits: Raman spectroscopic evidence for an  
745 important role of aqueous Sn (IV) species. *Geochimica et Cosmochimica Acta*, 220: 499-  
746 511.
- 747 Sheard, E.R., Williams-Jones, A.E., Heiligmann, M., Pederson, C., Trueman, D.L., 2012. Controls  
748 on the concentration of zirconium, niobium, and the rare earth elements in the Thor Lake  
749 rare metal deposit, Northwest Territories, Canada. *Economic Geology*, 107(1): 81-104.
- 750 Sun, S.-S., McDonough, W.F., 1989. Chemical and isotopic systematics of oceanic basalts:  
751 implications for mantle composition and processes. Geological Society, London, Special  
752 Publications, 42(1): 313-345.

- 753 Taylor, J.R., Wall, V.J., 1993. Cassiterite solubility, tin speciation, and transport in a magmatic  
754 aqueous phase. *Economic Geology*, 88(2): 437-460.
- 755 Trumbull, R., Garda, G., Xavier, R., Cavalcanti, J., Codeço, M.S., 2019. Tourmaline in the  
756 Passagem de Mariana gold deposit (Brazil) revisited: major-element, trace-element and B-  
757 isotope constraints on metallogenesis. *Mineralium Deposita*, 54(3): 395-414.
- 758 Trumbull, R.B., Beurlen, H., Wiedenbeck, M., Soares, D.R., 2013. The diversity of B-isotope  
759 variations in tourmaline from rare-element pegmatites in the Borborema Province of Brazil.  
760 *Chemical Geology*, 352: 47-62.
- 761 Trumbull, R.B., Codeço, M.S., Jiang, S.-Y., Palmer, M.R., Slack, J.F., 2020. Boron isotope  
762 variations in tourmaline from hydrothermal ore deposits: A review of controlling factors  
763 and insights for mineralizing systems. *Ore Geology Reviews*: 103682.
- 764 Turner, D., 1983. Upper Proterozoic schist belts in the Nigerian sector of the Pan-African Province  
765 of West Africa. *Precambrian research*, 21(1-2): 55-79.
- 766 Valley, P.M., Fisher, C.M., Hanchar, J.M., Lam, R., Tubrett, M., 2010. Hafnium isotopes in zircon:  
767 A tracer of fluid-rock interaction during magnetite–apatite (“Kiruna-type”) mineralization.  
768 *Chemical Geology*, 275(3-4): 208-220.
- 769 Vincent, V.I., Li, H., Girei, M.B., Ahmed, H.A., Ntekim, E.E., 2021. Genesis and age of PbZn  
770 mineralization from the Ningi-Burra ring complex, North Central Nigeria: Constraints  
771 from zircon morphology, UPb dating and LuHf isotopes. *Lithos*: 106115.
- 772 Vincent, V.I., Wang, L.-X., Zhu, Y.-X., Kamaunji, V.D., Ahmed, H.A., Ntekim, E.E., Cao, L.,  
773 2022. Onset of the anorogenic alkaline magmatism in the Nigerian Younger Granite  
774 province: Constraints from the Daura and Dutse complexes. *Lithos*, 410: 106561.

- 775 Viswanathan, S., Singh, Y., Mahabaleswar, B., 2012. Geochemical behaviour of vanadium,  
776 chromium, cobalt, nickel, and copper during progressive chloritization of biotites in  
777 granites. *Journal of the Geological Society of India*, 80(3): 301-303.
- 778 von Goerne, G., Franz, G., Heinrich, W., 2001. Synthesis of tourmaline solid solutions in the  
779 system  $\text{Na}_2\text{O}-\text{MgO}-\text{Al}_2\text{O}_3-\text{SiO}_2-\text{B}_2\text{O}_3-\text{H}_2\text{O}-\text{HCl}$  and the distribution of Na  
780 between tourmaline and fluid at 300 to 700 C and 200 MPa. *Contributions to Mineralogy  
781 and Petrology*, 141(2): 160-173.
- 782 von Goerne, G., Franz, G., van Hinsberg, V.J., 2011. Experimental determination of Na–Ca  
783 distribution between tourmaline and fluid in the system  $\text{CaO}-\text{Na}_2\text{O}-\text{MgO}-\text{Al}_2\text{O}_3-\text{SiO}_2-$   
784  $\text{B}_2\text{O}_3-\text{H}_2\text{O}$ . *The Canadian Mineralogist*, 49(1): 137-152.
- 785 Wang, J.-X., Nie, F.-J., Zhang, X.-N., Jiang, S.-H., 2016. Molybdenite Re–Os, zircon U–Pb dating  
786 and Lu–Hf isotopic analysis of the Xiaerchulu Au deposit, Inner Mongolia Province, China.  
787 *Lithos*, 261: 356-372.
- 788 Winderbaum, L., Ciobanu, C.L., Cook, N.J., Paul, M., Metcalfe, A., Gilbert, S., 2012. Multivariate  
789 analysis of an LA-ICP-MS trace element dataset for pyrite. *Mathematical Geosciences*,  
790 44(7): 823-842.
- 791 Yang, S.-Y., Jiang, S.-Y., Zhao, K.-D., Dai, B.-Z., Yang, T., 2015. Tourmaline as a recorder of  
792 magmatic–hydrothermal evolution: an in situ major and trace element analysis of  
793 tourmaline from the Qitianling batholith, South China. *Contributions to Mineralogy and  
794 Petrology*, 170(5): 1-21.
- 795 Zhang, W., Chen, H., Peng, L., Zhao, L., Huang, J., Lu, W., Liang, P., Lai, C., 2018.  
796 Discriminating hydrothermal fluid sources using tourmaline boron isotopes: Example from

797 Bailingshan Fe deposit in the Eastern Tianshan, NW China. *Ore Geology Reviews*, 98: 28-  
798 37.

799 Zhao, H.-D., Zhao, K.-D., Palmer, M.R., Jiang, S.-Y., Chen, W., 2021a. Magmatic-Hydrothermal  
800 Mineralization Processes at the Yidong Tin Deposit, South China: Insights from In Situ  
801 Chemical and Boron Isotope Changes of Tourmaline. *Economic Geology*, 116(7): 1625-  
802 1647.

803 Zhao, K.-D., Zhang, L.-H., Palmer, M.R., Jiang, S.-Y., Xu, C., Zhao, H.-D., Chen, W., 2021b.  
804 Chemical and boron isotopic compositions of tourmaline at the Dachang Sn-polymetallic  
805 ore district in South China: Constraints on the origin and evolution of hydrothermal fluids.  
806 *Mineralium Deposita*, 56: 1589–1608.

807 Zhao, Z., Yang, X., Zhang, T., Lu, Y., Li, W., Zhang, Z., 2022. Geochemical characteristics and  
808 boron isotopes of tourmaline from the Baishaziling tin deposit, Nanling Range: Constraints  
809 on magmatic-hydrothermal processes. *Ore Geology Reviews*, 142: 104695.

## 810 **Figure Captions**

811

812 **Fig. 1.** Geological sketch map showing (a) generalized map of Africa showing the distribution of  
813 rare-metal granites and rare metal-bearing pegmatites. (b) Nigeria showing distribution of Pan-  
814 African granites, schist belts, and established NE-SW trending Sn-W bearing pegmatites. The  
815 Raghane shear zone is a potential suture zone marking the boundary between Eastern Nigeria  
816 Terrane (ENT) and Western Nigeria Terrane (WNT) adopted from Ferré et al. (1998).

817

818 **Fig. 2.** Geological map of (a) the Bin Yauri-Libata area showing the distribution of Au and Sn  
819 mineralizations, and (b) the Libata Sn ore field showing the distribution of ore-bearing lodes.

820

821 **Fig. 3.** Photographs showing hand specimens and photomicrographs (PPL) of (a) deformed granite  
822 porphyry; (b) altered biotite granite wall rock sample from vein 1; (c) hand specimen  
823 photomicrograph of quartz vein-hosted hydrothermal tourmaline from Libata vein 1; (d) wall rock  
824 from the granite-hosted vein 1 showing the occurrence of unzoned and zoned tourmaline; (e) quartz  
825 vein-hosted hydrothermal tourmaline from Libata vein 2 and (f) tourmaline and zircon from wall  
826 rock sections at the Libata vein 2; (g) section from quartz vein at Libata vein 2 and (h) wall rock  
827 alteration zone from Libata vein 2. Abbreviation: Ab, albite; Fe-Ti oxides, iron-titanite oxides; Kfs,  
828 K-feldspar; Ms, muscovite; Plg, plagioclase; Py, pyrite; Qtz, quartz; Tur, tourmaline; Zr, zircon.

829 **Fig. 4.** (a) Selected BSE-images of analyzed sections from veins 1 and 2 in the Libata ore field.  
830 SEM micrographs of the bulk ore showing distinct morphologies of (b) albite grains occurring  
831 with K-feldspar and quartz from wall rocks near vein 1; (c) tourmaline from vein 2 with later-stage  
832 K-feldspar; (d) tourmaline-chlorite occurrence seen in vein 1; (e) chlorite-tourmaline-quartz  
833 assemblage from Libata vein 1. Abbreviation: Ab, albite; Chl, chlorite; Kfs, K-feldspar; Tur,  
834 tourmaline; Qtz, quartz.

835

836 **Fig. 5.** Simplified paragenesis for the Libata Sn mineralizations. The thickness of the horizontal  
837 lines indicates the abundance of the mineral species.

838

839 **Fig. 6.** Selected CL-images of analyzed zircon grains from the (a) granite porphyry (CR-01) and  
840 (b) altered biotite granite (KB-01). (c) Representative transmitted and reflected light images of  
841 zircons, showing the distribution of fluid/mineral inclusions in the granite porphyry and altered  
842 biotite granite samples.

843

844 **Fig. 7.** Magmatic-hydrothermal zircon discrimination plots of (a) SmN/LaN vs. Ce/Ce\* diagram;  
845 (b) La vs. SmN/LaN diagram. (c) Ti vs LREE-I showing LREE+Ti contamination as well as  
846 potential contamination by Ti without substantial LREE. (d) Hf vs LREE-I showing both a positive  
847 correlation expected for magmatic zircon grains and alteration trend for the hydrothermally altered  
848 zircon grains. Fig. 7(c-d) adapted from Bell et al., 2019. Magmatic-hydrothermal zircon plots for  
849 (e)  $\Sigma$ REE vs.  $\Sigma$ LREE; and (f)  $\Sigma$ REE vs. Eu/Eu\* values in zircon grains from the Libata Sn  
850 mineralization. Magmatic and hydrothermal fields are from Hoskin (2005).

851

852 **Fig. 8.** Zircon U-Pb concordant ages of different zircon groups in the (a-b) granite porphyry (CR-  
853 01), and (c-d) altered biotite granite (KB-01) samples. Group 1 zircons = magmatic zircons and  
854 Group 2 zircons = hydrothermally altered zircons. Chondrite-normalized REE patterns for the (e)  
855 granite porphyry and (f) altered biotite granite from the Libata quartz-tourmaline-cassiterite ore  
856 field. Normalization values for zircon/chondrite REE patterns are from Sun and McDonough  
857 (1989).

858

859 **Fig. 9.** Chemical compositions of tourmaline from Libata (a) Ca-X□-Na+K (apfu) ternary  
860 diagrams, after Henry et al. (2011); (b) Ca-Fe-Mg (apfu) ternary diagrams, after Henry and  
861 Guidotti (1985). Fig. 8 (c-d). Trace element and chondrite-normalized REE compositions of  
862 tourmalines from the Libata ore field. Fig. 8 (e-f). Principal component analysis (PCA) of LA-  
863 ICP-MS log-transformed trace element data from the Libata tourmaline (n = 49 spot analyses, 15  
864 variables). Trace element normalized to upper continental crust values (UCC) from Rudnick and  
865 Gao (2003) and normalization values for chondrites are from Sun and McDonough (1989).

866

867 **Fig. 10.** Frequency histogram of boron isotopic compositions of the (a) vein 1 tourmaline and vein  
868 2 tourmaline at Libata. (b)  $\delta^{11}\text{B}$  values of the tourmaline in the Libata Sn deposit. The  $\delta^{11}\text{B}$  data  
869 for boron reservoirs are cited from Marschall and Jiang (2011).  $\delta^{11}\text{B}$  data for deposits are from  
870 Ludwig et al. (2011); Codeço et al. (2017); Zhang et al. (2018); Trumbull et al. (2019) and  
871 Trumbull et al. (2020).

872

873 **Fig. 11.** Magmatic zircon geochemical diagrams for the Libata granites: (a) U/Yb vs. Yb, after  
874 Grimes et al. (2007) and (b)  $\text{Log}_{10}(\text{U}/\text{Yb})$  vs  $\text{Log}_{10}(\text{Nb}/\text{Yb})$  after Grimes et al. (2015).

875

876 **Fig. 12.** Hafnium isotopic signatures of different types of zircons (a) age vs.  $\epsilon\text{Hf}(t)$  scattered  
877 diagram for different zircons and neighboring deposits; (b) a limited age between 600 and 670 Ma  
878 of (a). (c)  $^{176}\text{Hf}/^{177}\text{Hf}$  vs.  $^{176}\text{Lu}/^{177}\text{Hf}$  and (d)  $^{176}\text{Hf}/^{177}\text{Hf}$  vs.  $^{176}\text{Yb}/^{177}\text{Hf}$ . Hf isotope values for the  
879 Archean basement complex rocks of Western Nigeria and West Africa are from Dickin et al.  
880 (1991), Ganade et al. (2016) and Petersson et al. (2018). Hf isotope values from the Benin-Nigeria  
881 shield are from Ganade et al. (2016) and Petersson et al. (2018), values for the Hawal Massif are  
882 from Bute et al. (2019), and values for the Brasilliano-Pan African orogeny are from Ganade et al.  
883 (2014).

884

885 **Fig. 13.** (a-b) Source discrimination plots for the Libata tourmalines based on Li/Sr ratio as  
886 compared to compositions of worldwide tourmaline hosted in granites and metamorphic rocks.  
887 Variation diagrams of selected trace elements in tourmaline from the Libata Sn ore field. (c) Sn vs.  
888 Co/La; (d) Sn vs. Zn/Nb. Data for Cornwall granites are from Duchoslav et al. (2017); Puy-les  
889 Vigness gneisses are from Harlaux et al. (2019); Hutti amphibolites are from Hazarika et al. (2015);

890 Dachang granite-hosted Sn deposit are from Zhao et al. (2021b) and Baishaziling granite-hosted  
891 Sn deposit are from Zhao et al. (2022). Field for tourmaline hosted in granites, metasediments and  
892 metavolcanic rocks is from Harlaux et al. (2019). Field for tourmaline hosted in barren vs  
893 mineralized granite from Hong et al. (2017).

894

895 **Fig. 14.** Scatter diagrams of zircon LA-ICP-MS results (ppm). (a)  $Y + \Sigma\text{REE}$  vs.  $U + \text{Nb} + \text{Ta}$ ; (b)  
896  $Y + \Sigma\text{REE}$  vs.  $\text{Th}/U$ ; (c)  $Y/\text{Ho}$  vs.  $Y.$ ; and (d)  $\text{Eu}/\text{Eu}^*$  vs.  $\text{Yb}/\text{Gd}$ . C1-Chondritic value of  $Y/\text{Ho} =$   
897 28 in (c) from Bau (1996). Dashed line at  $\text{Eu}/\text{Eu}^*$  represent demarcation of field of fertile and  
898 barren granites. Values for fertile and infertile Phanerozoic granites are from Lu et al. (2019).

### 899 **Table Caption**

900 Table 1. Major distinct characteristics of zircon types from granites in the Libata Sn-W orefield.

901 Table 2. LA-ICP-MS Zircon U-Pb data of the studied granites.

902 Table 3. Zircon in situ Lu-Hf isotopic compositions of the Libata granites.

### 903 **Online Material Caption**

904 Online Material<sup>1</sup> Description of analytical methods

905 Online Material<sup>2</sup> Table OM1 Zircon trace element compositions of the Libata granites

906 Online Material<sup>3</sup> Table OM1 Major element compositions from tourmalines in the Libata tin ore  
907 district.

908 Online Material<sup>3</sup> Table OM2 Trace element compositions from tourmalines in the Libata tin ore  
909 district.



910 Online Material<sup>3</sup> Table OM3 LA-ICP-MS Boron isotope analysis from the Libata Sn-W ore field.

911 Online Material<sup>4</sup> Table OM1 Zircon U-Pb data for standard samples GJ-1 and PLE.

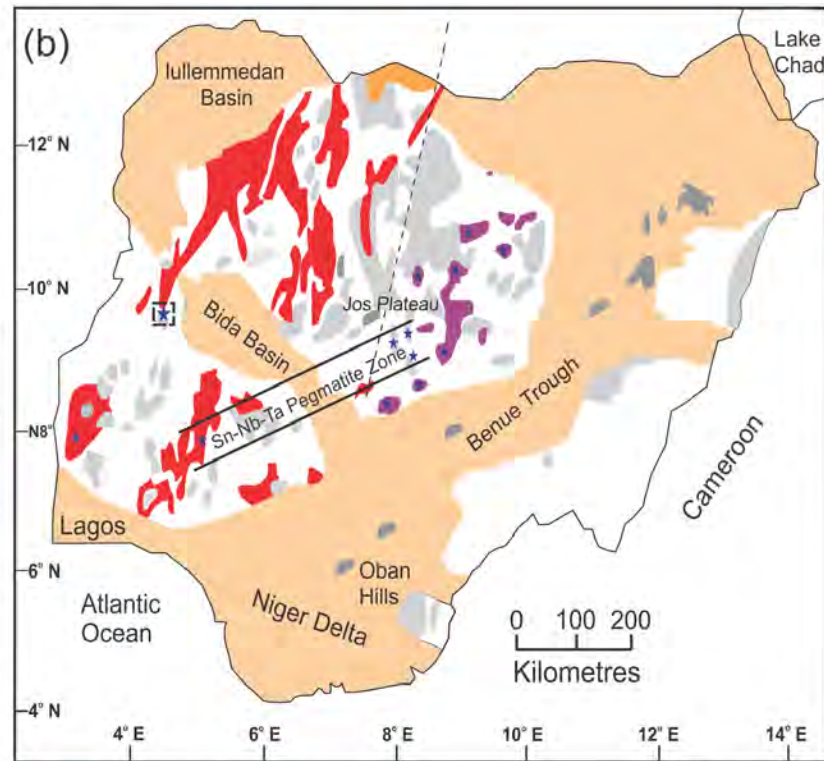
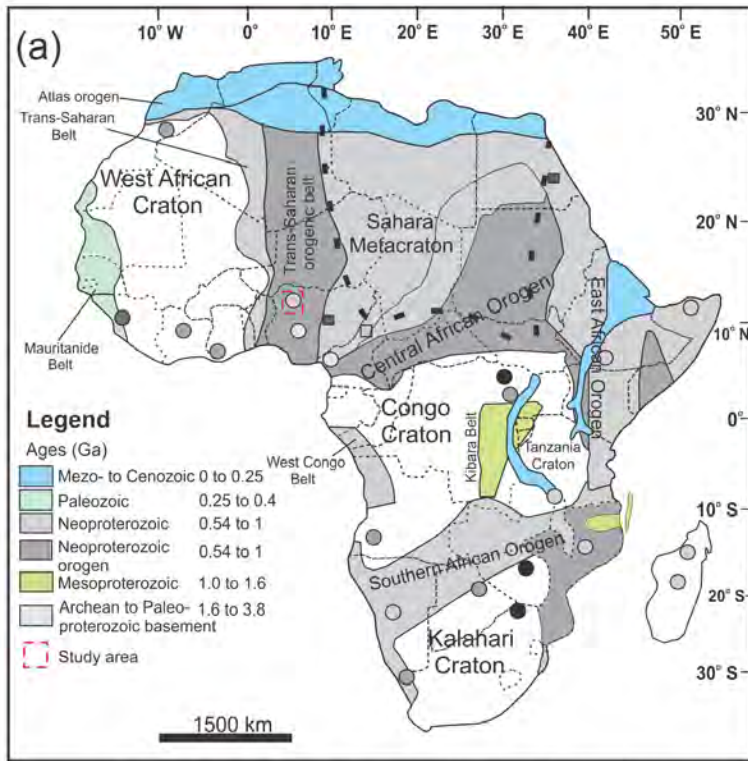
912 Online Material<sup>4</sup> Table OM2 Zircon trace element data for standard samples GJ-1 and PLE.

913 Online Material<sup>4</sup> Table OM3 Trace element analytical results of standard sample BCR-2G, BIR-  
914 1G and BVHO-2G.

915 **Supplementary Figure captions**

916

917 Supplementary Figure 1. Zircon U-Pb concordia for standard zircon samples GJ-1 and the  
918 Plesovice (PLE).



**Rare-metal granite and Rare-element pegmatite province**

- Rare-metal granite province
- Rare-elemental pegmatite province
- Mesozoic
- Paleozoic
- Paleoproterozoic
- Archean

- Cretaceous - Recent sedimentary basins
- Older granites
- Volcanics
- Younger granites
- Schist belts
- Migmatite gneiss
- ★ Study Area
- ★ Sn-Nb-Ta-W mineralization

**Figure 1**

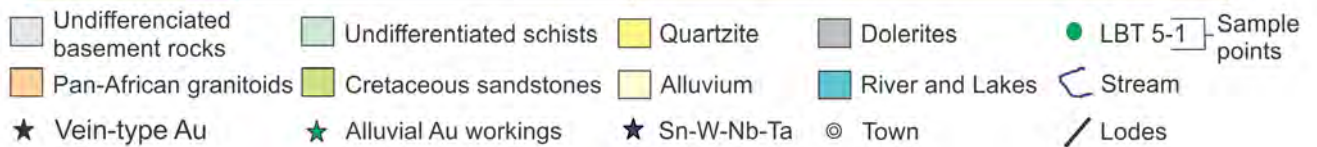
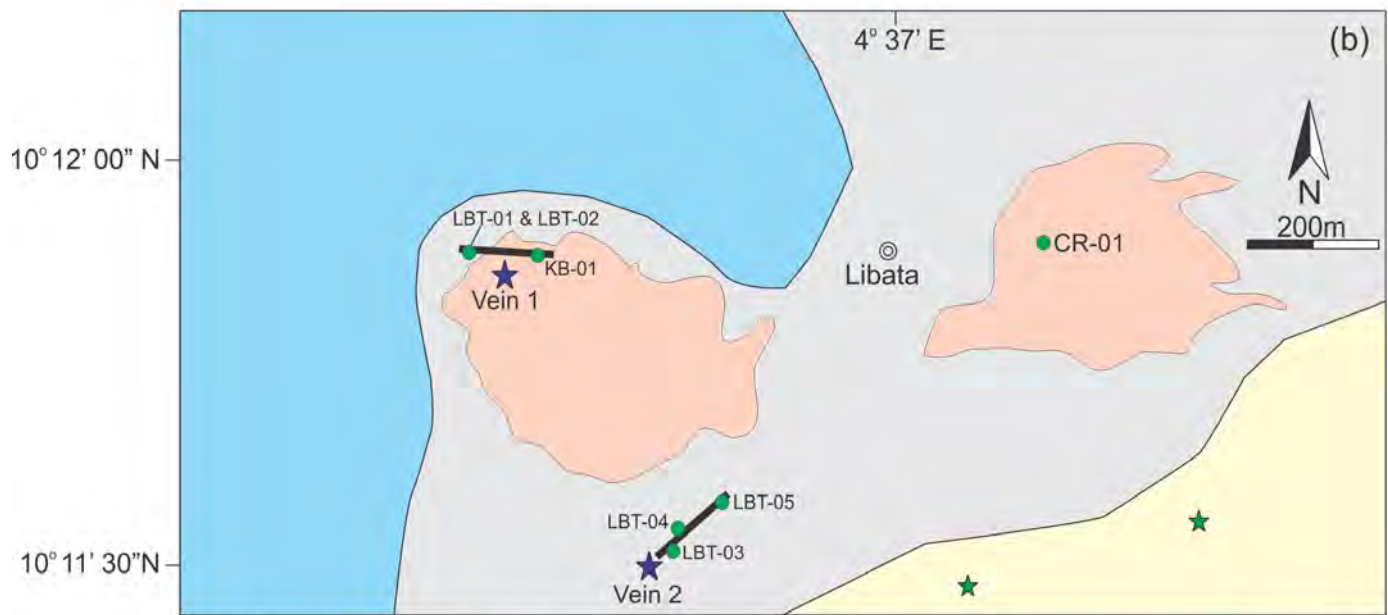
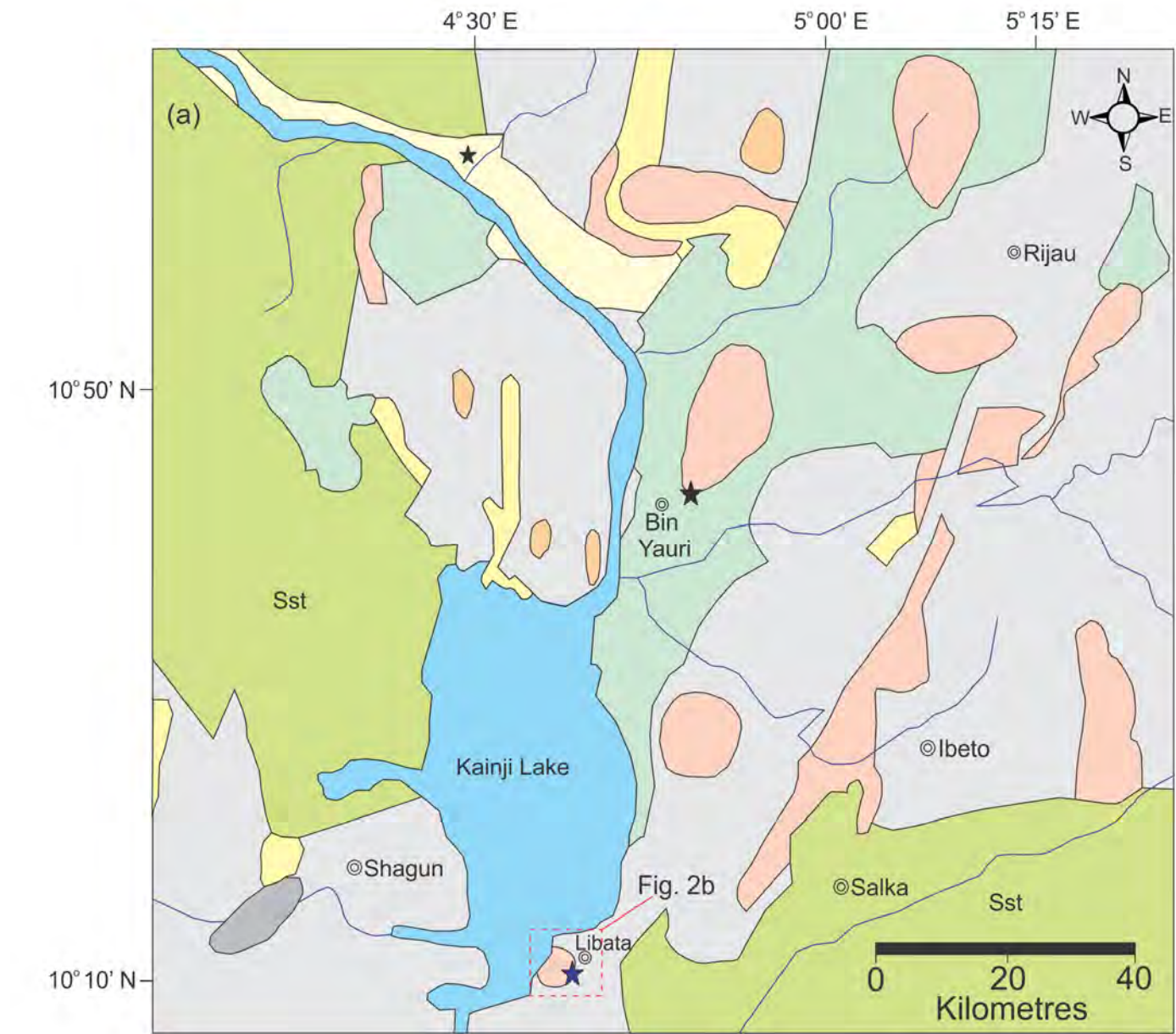


**Figure 2**

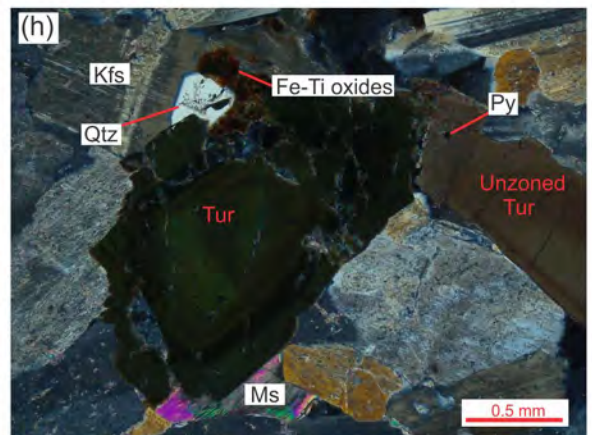
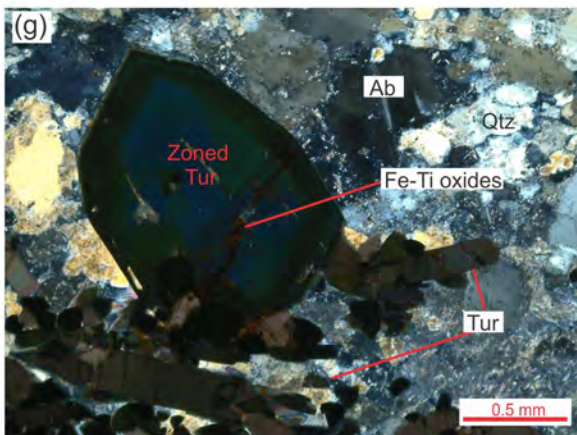
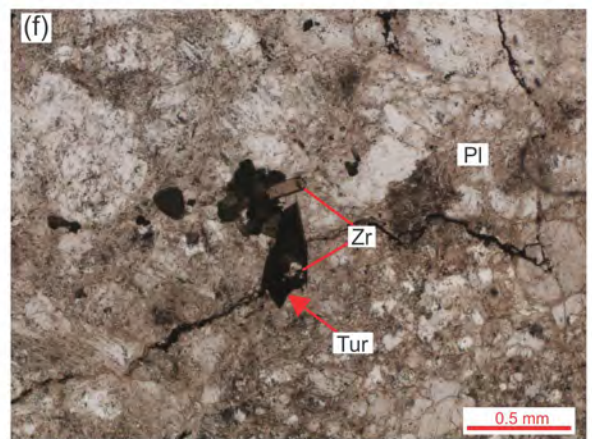
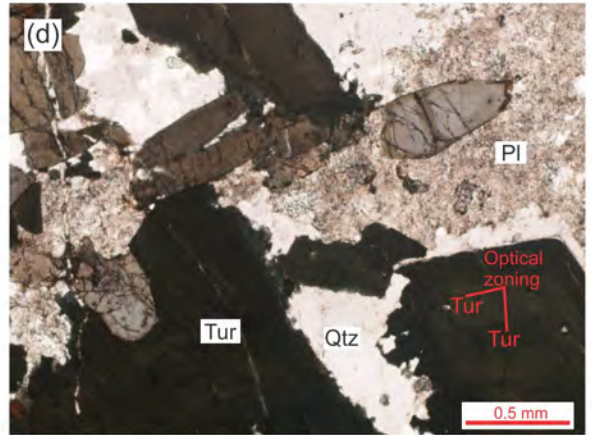
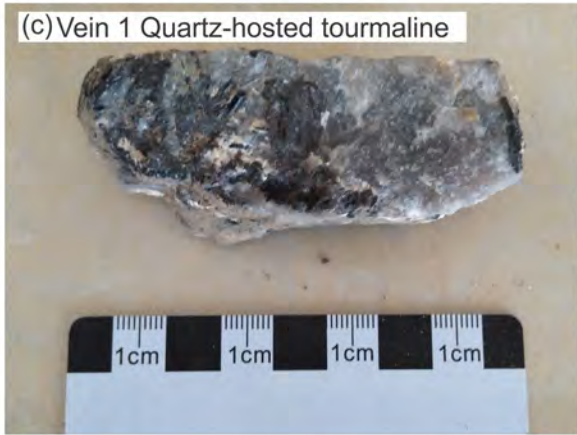
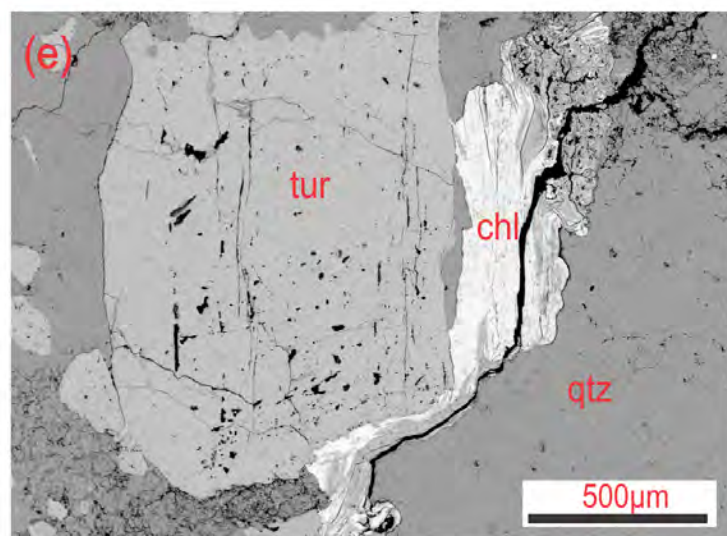
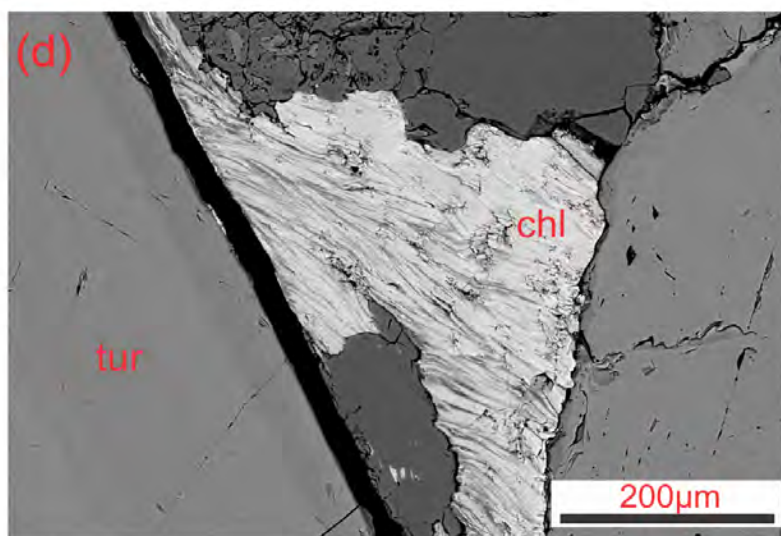
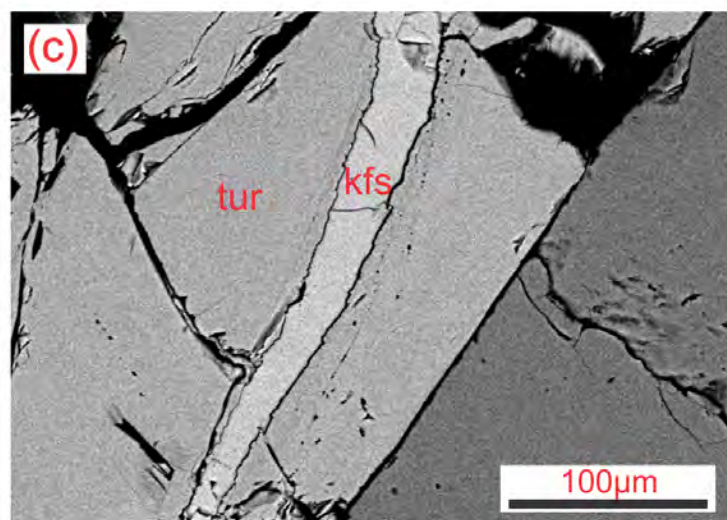
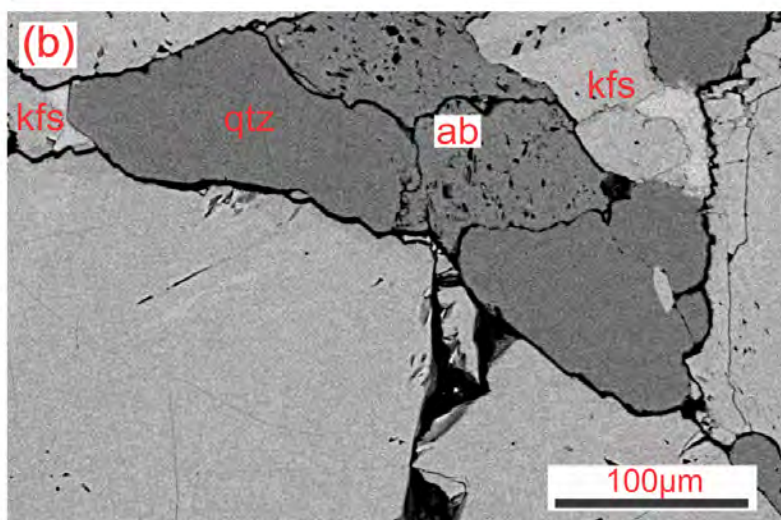
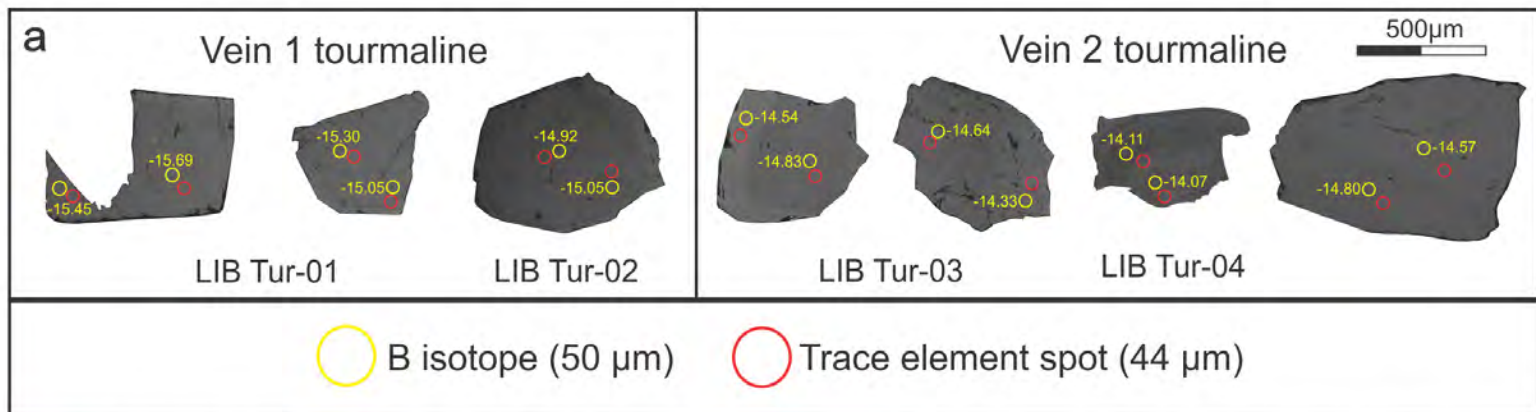
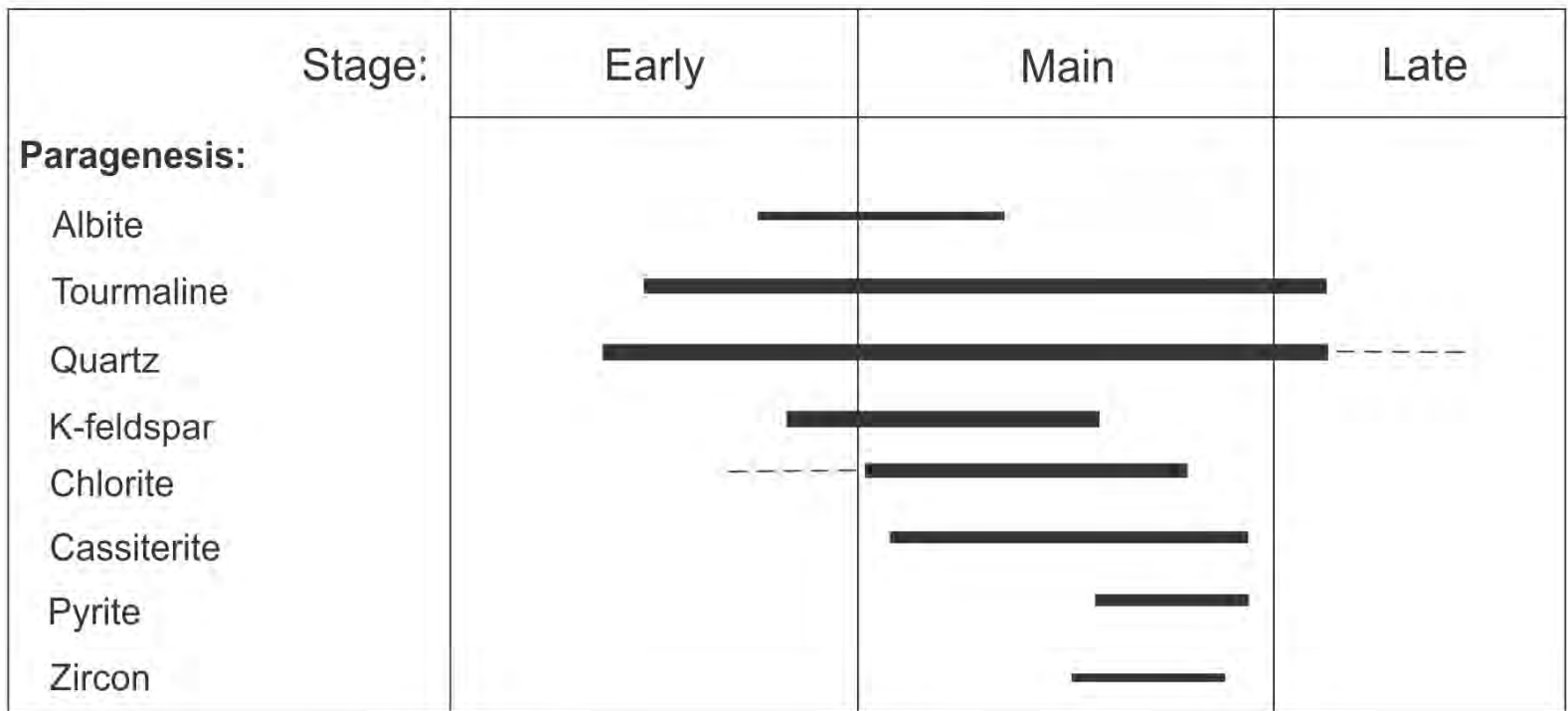


Figure 3



**Figure 4**



Abundant
  Minor
  Trace

**Figure 5**

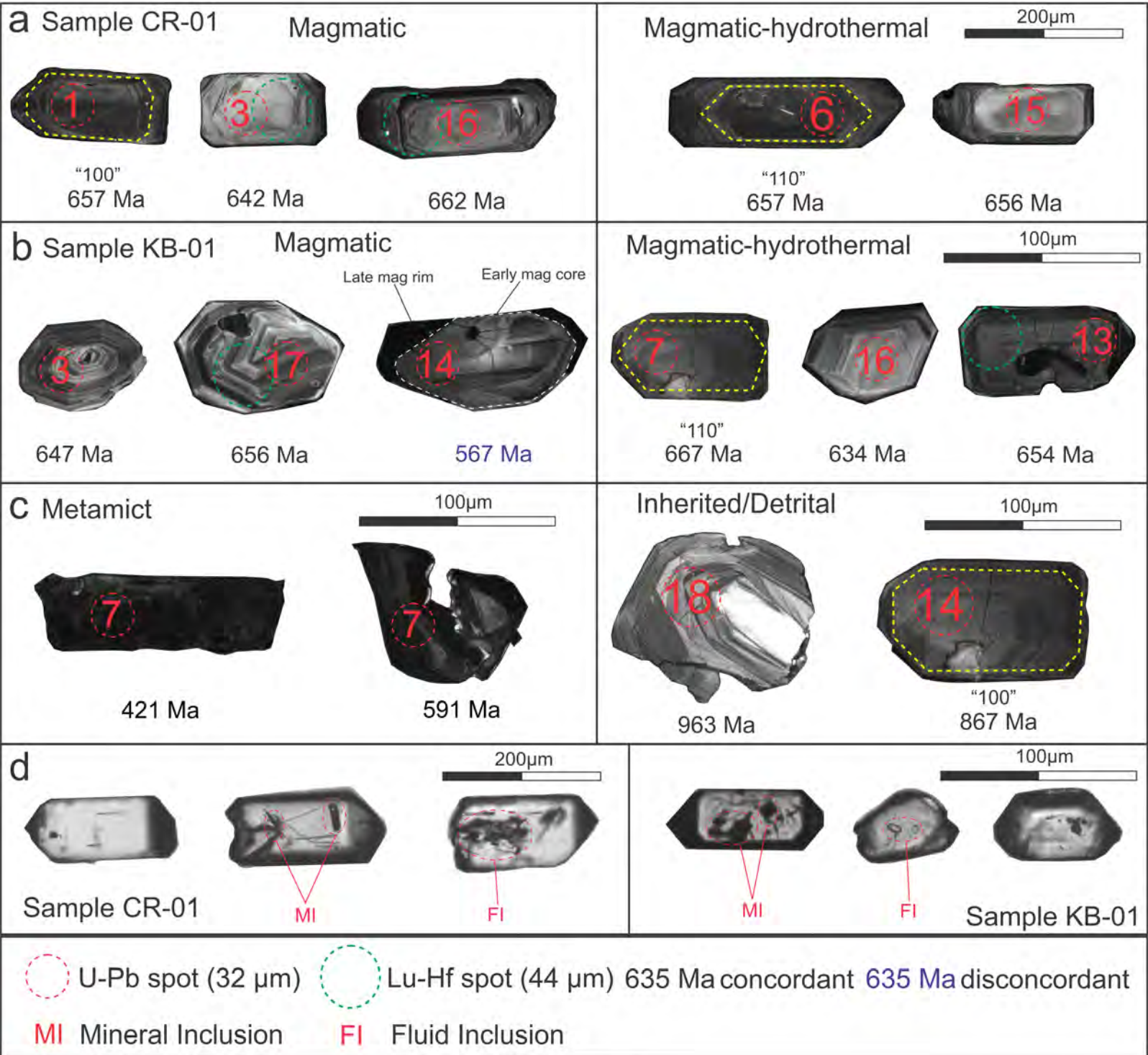


**Figure 6**

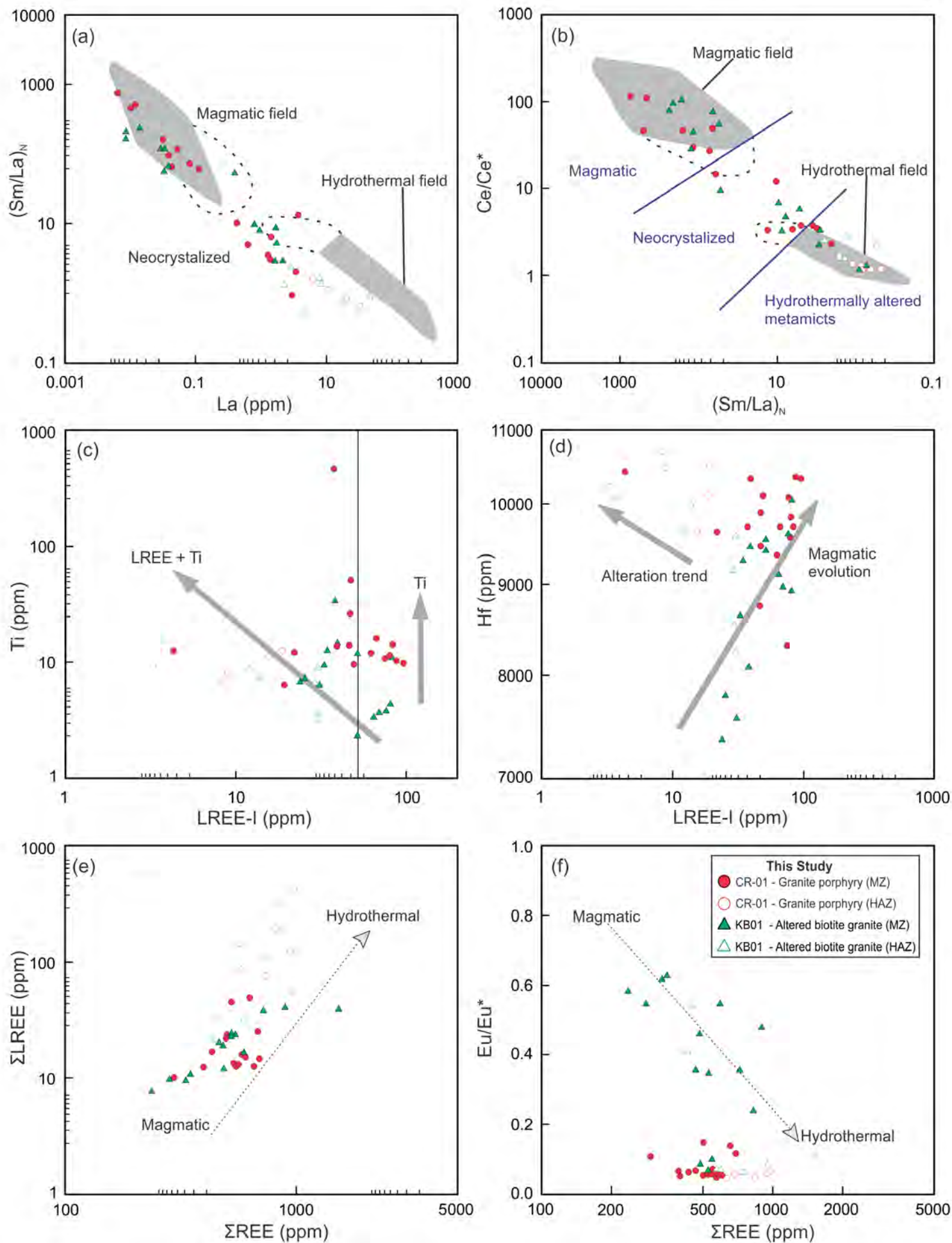
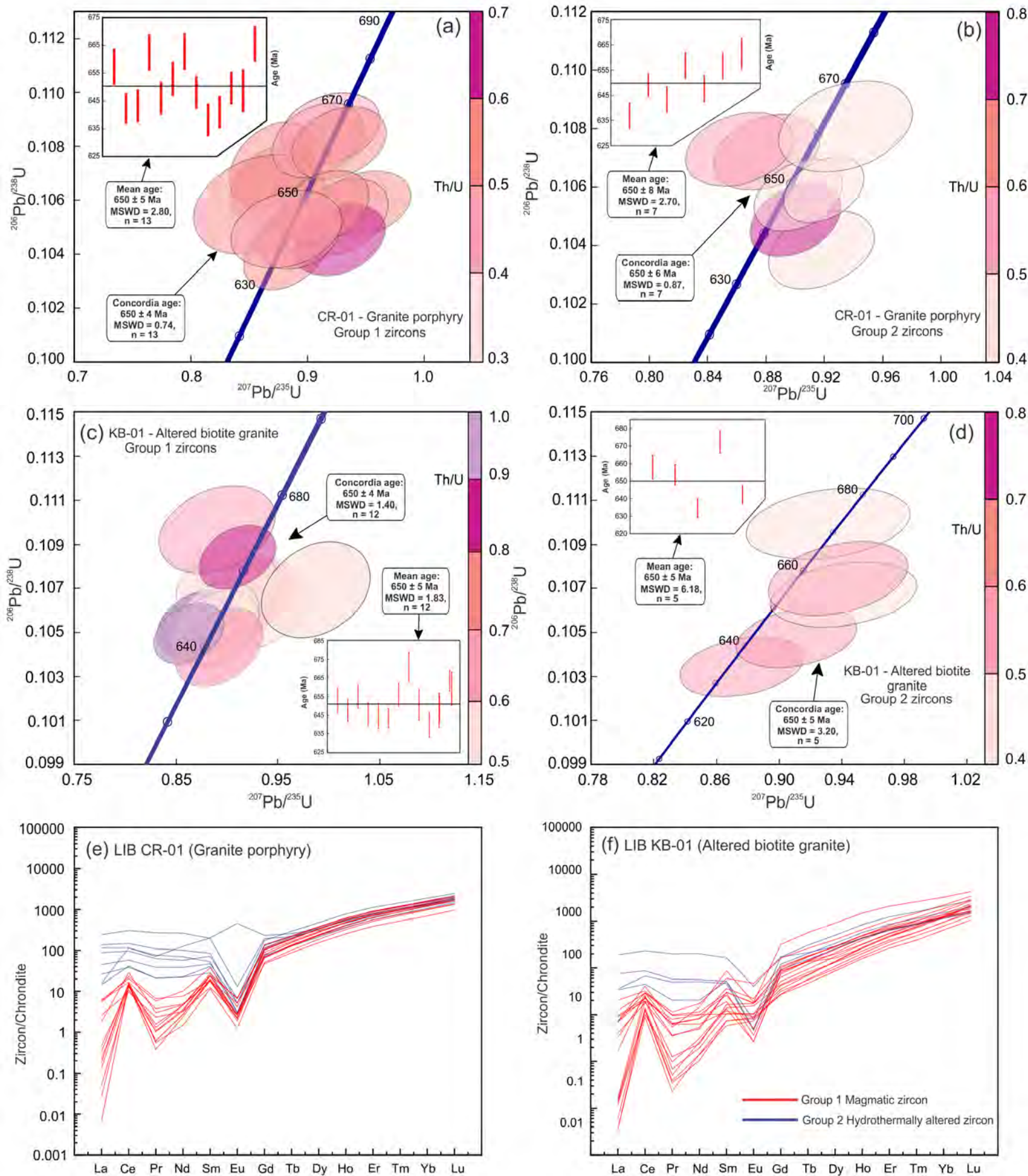
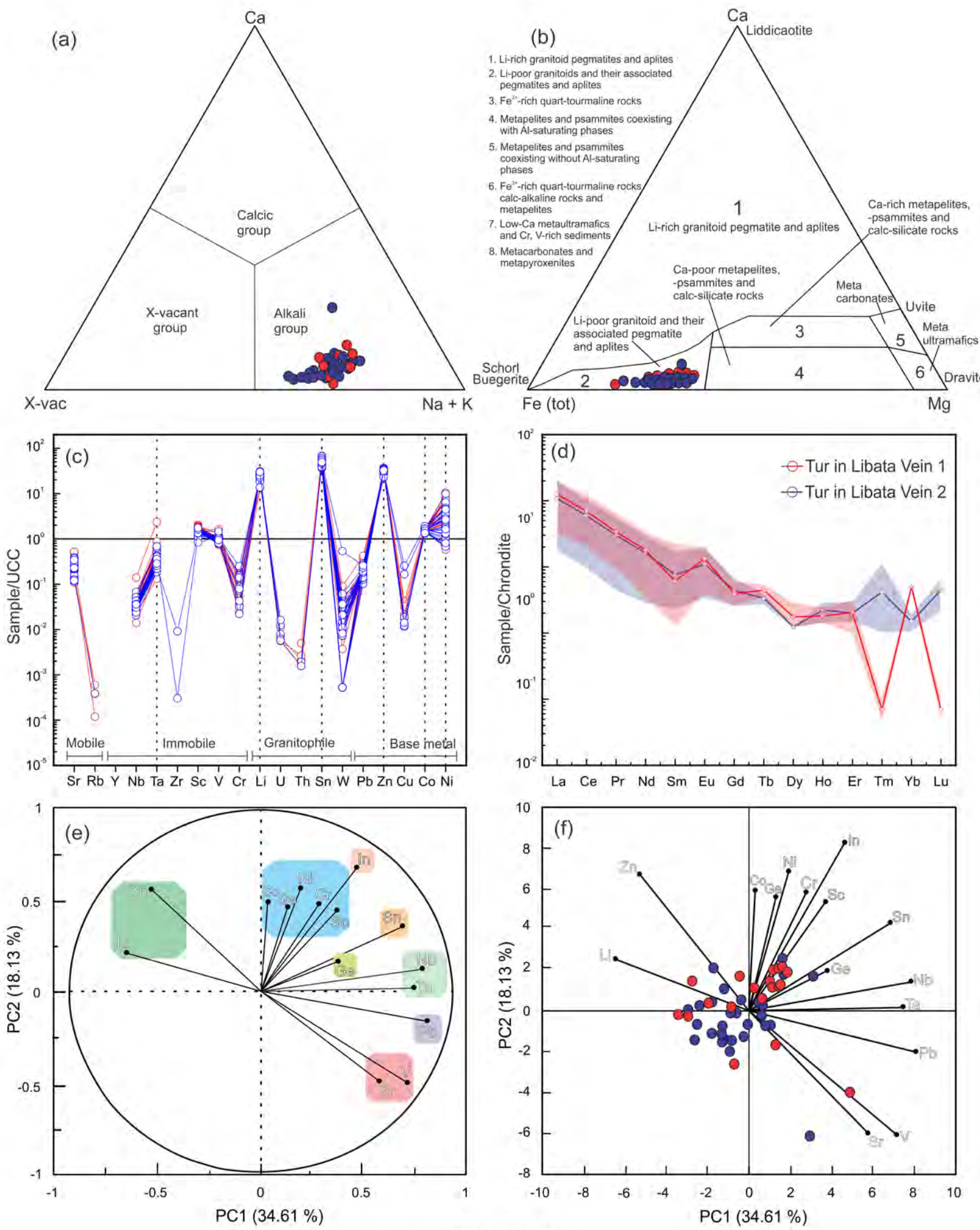


Figure 7



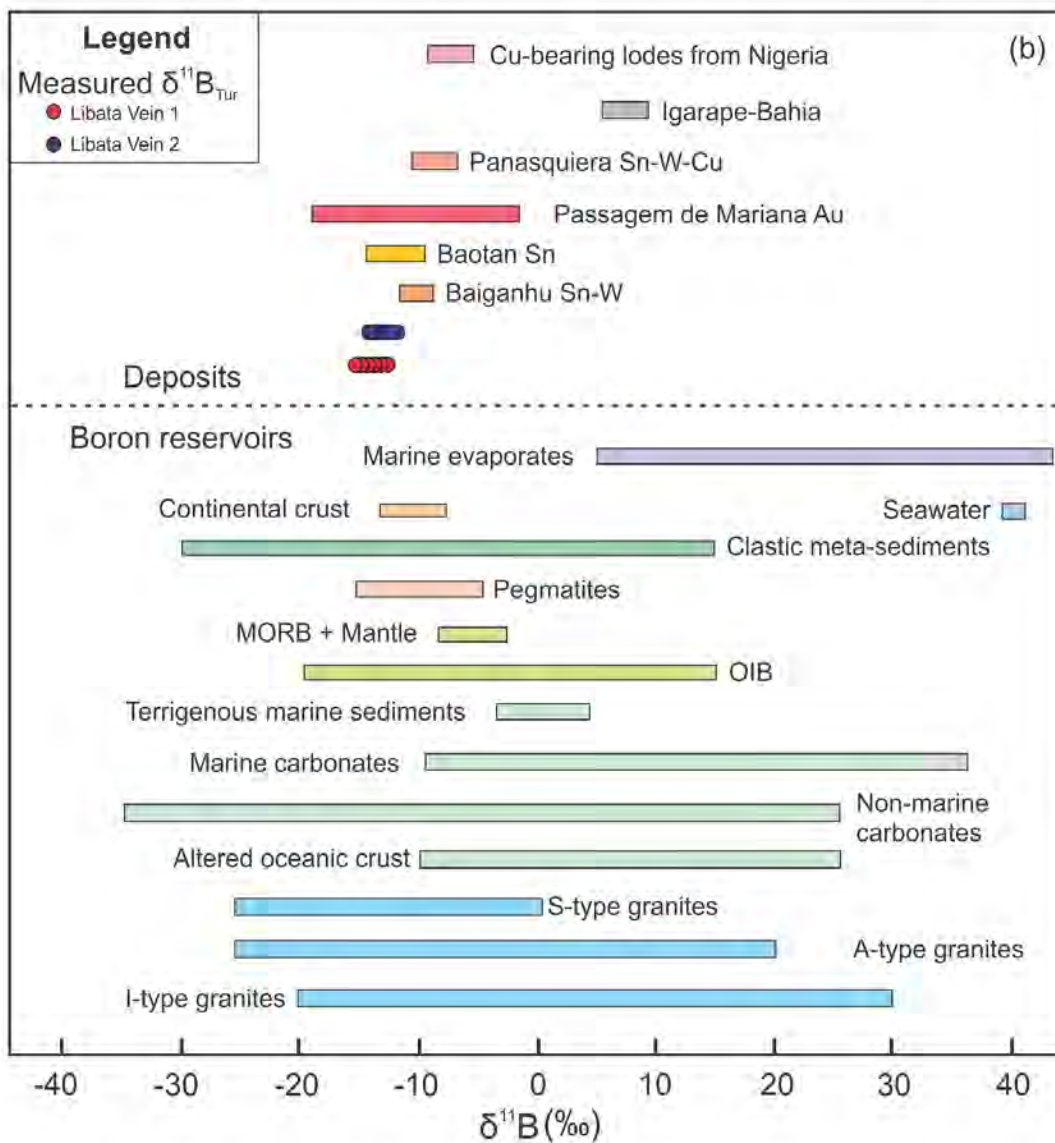
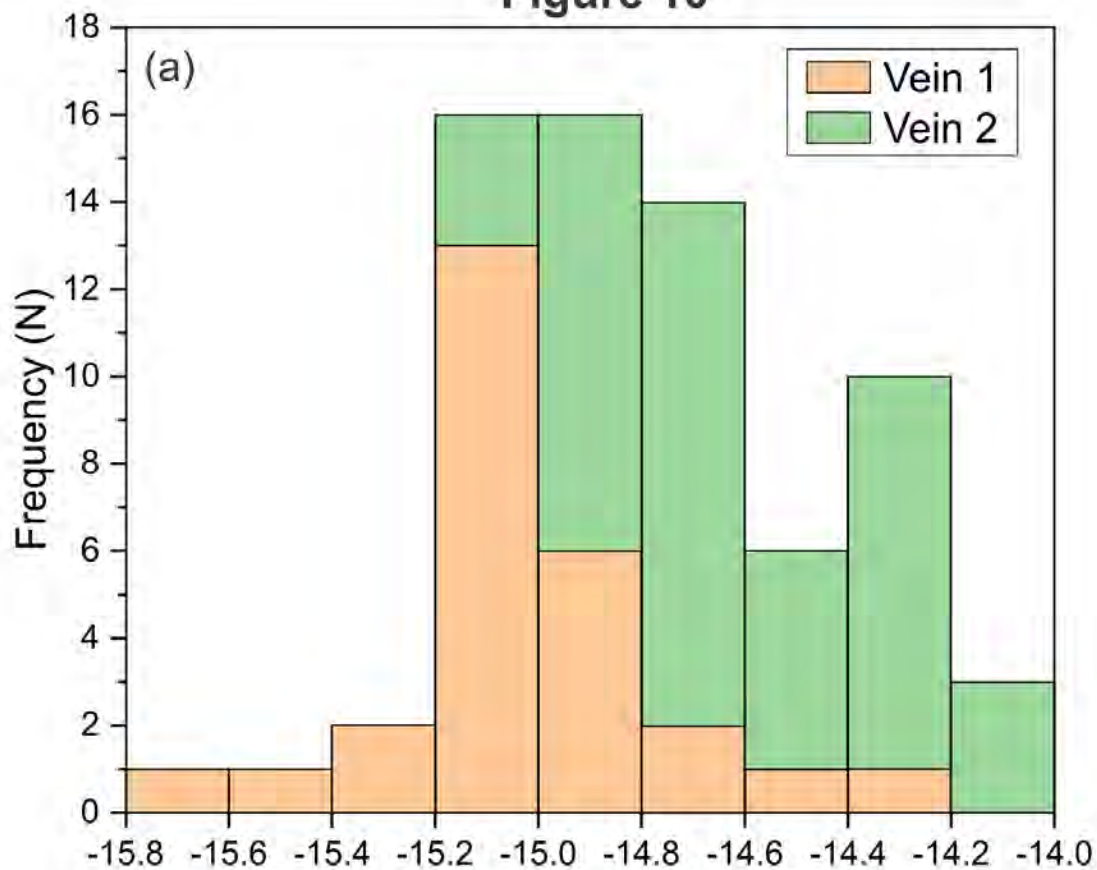


**Figure 8**



**Figure 9**

**Figure 10**



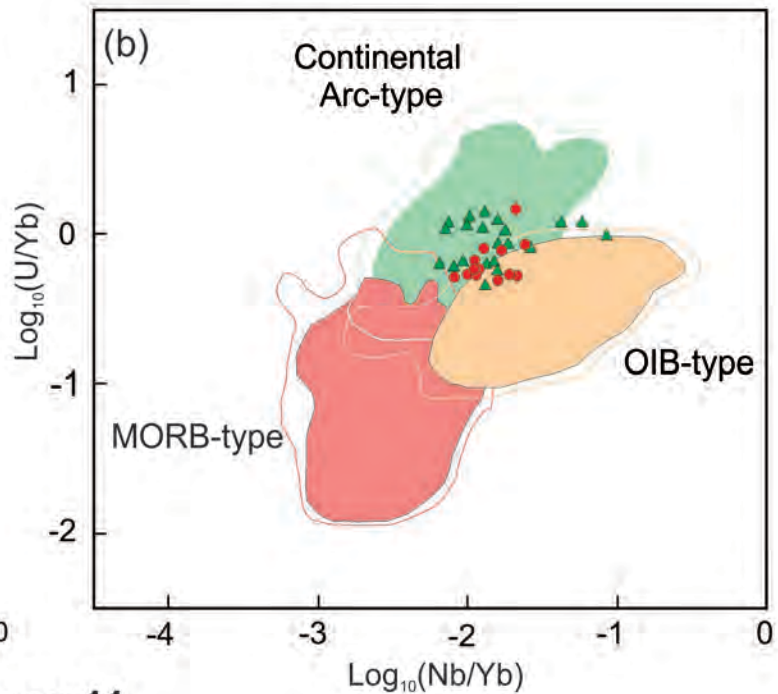
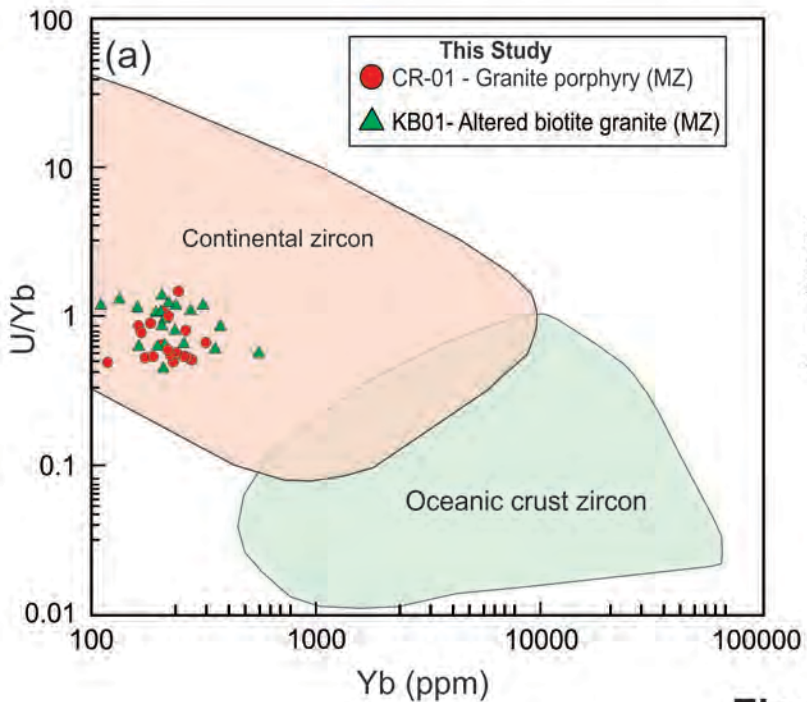


**Figure 11**

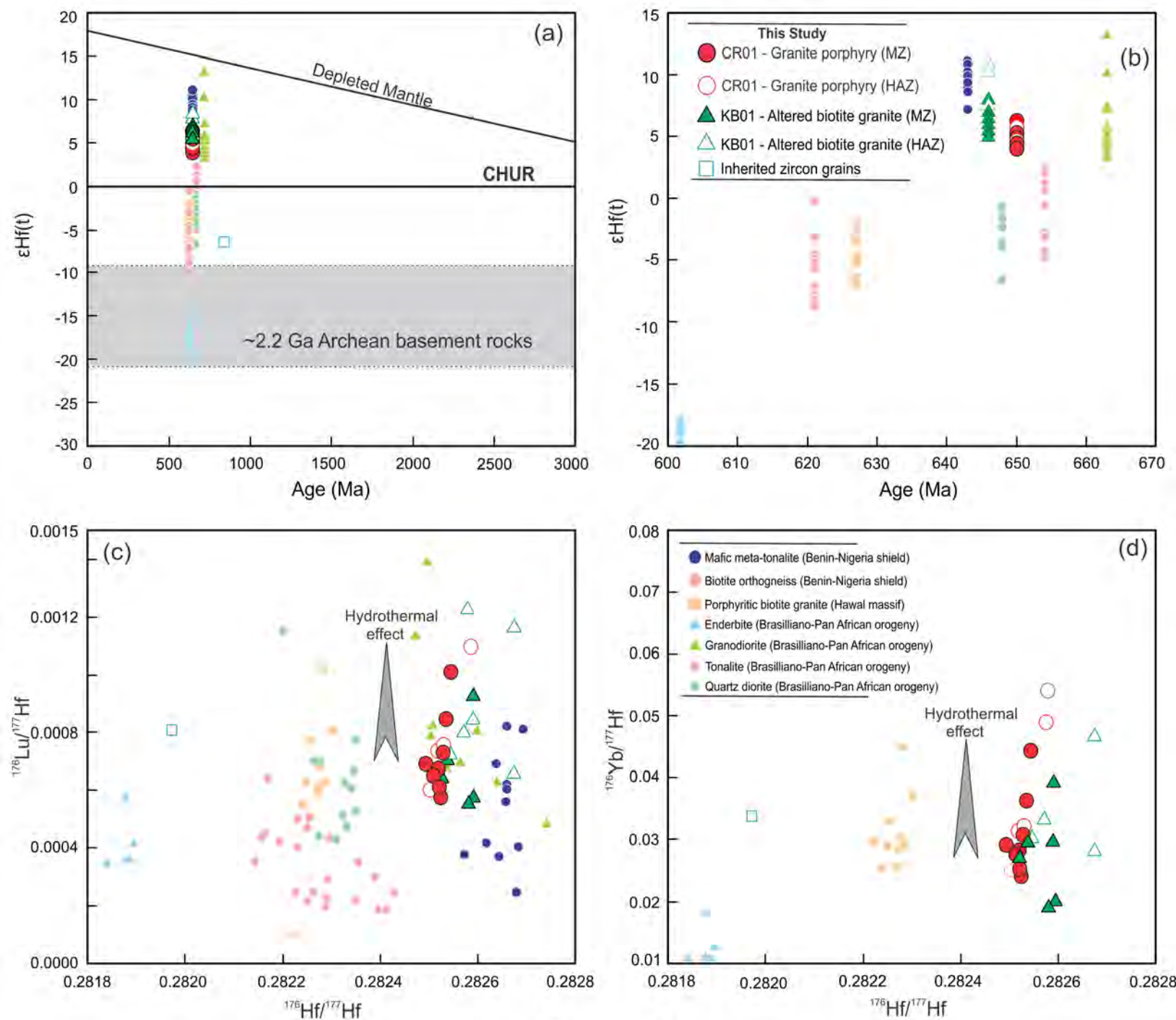


**Figure 12**

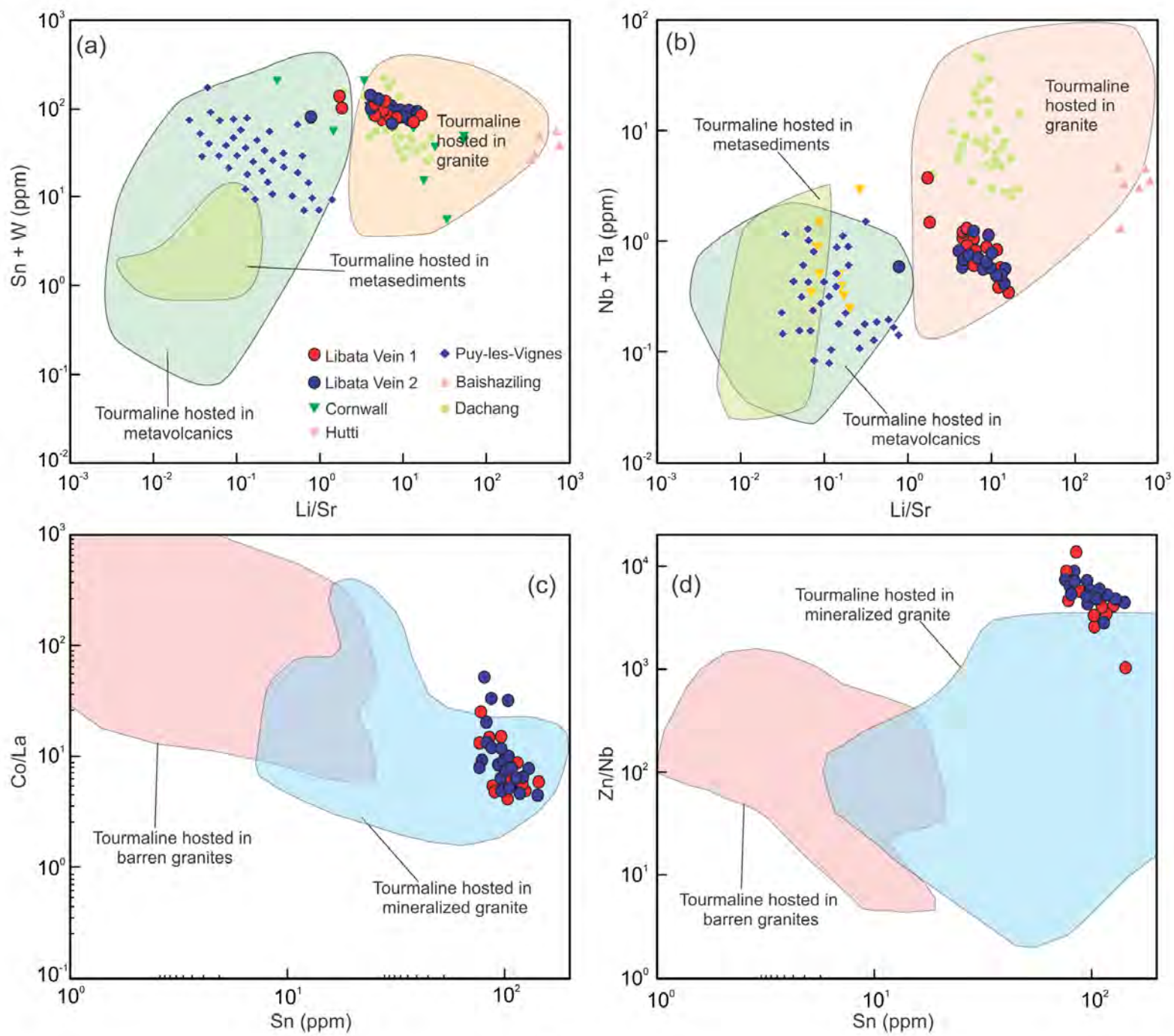
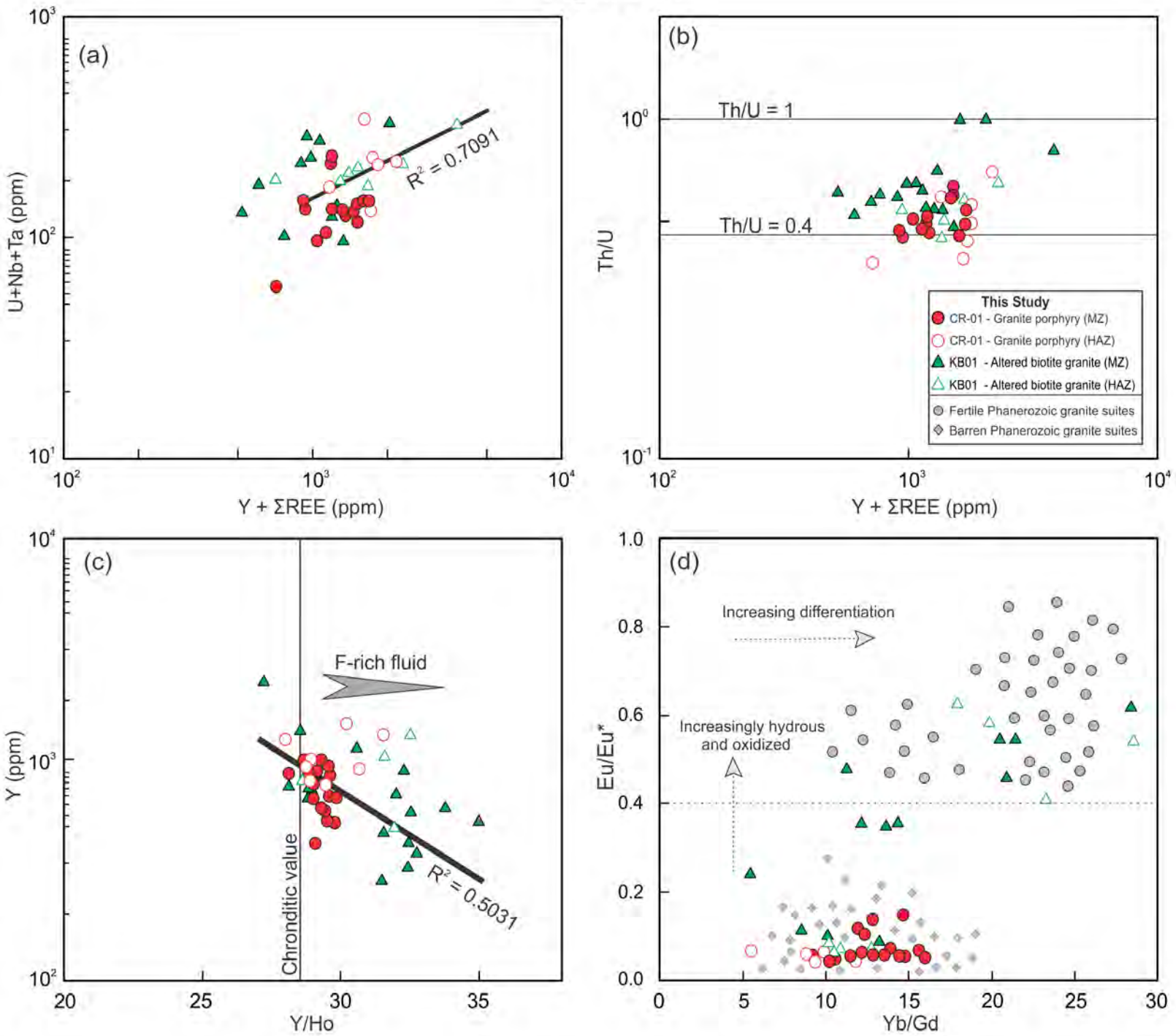


Figure 13

Figure 14



**Table 1. Major distinct characteristics of zircon types from granites in the Libata Sn orefield**

Character/type	Magmatic	Hydrothermally-altered	Inherited
Size	50-300 $\mu\text{m}$	50-200 $\mu\text{m}$	100-150 $\mu\text{m}$
Morphology	Euhedral & anhedral Dominant {100} with minimal {110} prism face	Euhedral & subeuhedral Dominant {110} prism face	Subhedral & anhedral Dominant {100} prism face
Optical appearance	Transparent and colorless	Murky-brown opaque	Transparent and colorless
CL appearance	High intensity Clear zoned texture	Low intensity Variable with zoned and unzoned grains	High intensity Variable with zoned and unzoned grains
Formation mechanism	Early- and late-stage magmatic melt	Early magmatic melt and altered by hydrothermal fluid	Mostly ancient magmatic melt (distinct zircon ages)
Internal structure	Inclusion-poor Fracture-poor	Inclusion-rich Fracture-rich Spongy texture	Inclusion-poor Fracture-poor
Geochemical feature	Moderate negative Eu anomaly Strong positive Ce anomaly Depleted in LREE Low common Pb content	Strong negative Eu anomaly Flat Ce anomaly trends Strongly enriched in U, Th, Y, REE, Nb Moderately enriched in Ti, Sc, Pb, Hf, Ta High common Pb content & varying degree of radiogenic Pb loss	Moderate negative Eu anomaly Strong Ce anomaly Depleted in LREE Low common Pb content
Zircon grain U-Pb ages	~650 Ma	~650 Ma	>800 Ma
Lu-Hf isotope signature	+4.4 to	+4.5 to +10.6	-7.63



**Table 2. LA-ICP-MS Zircon U-Pb data for the studied granites.**

Sample No	Type	Isotopic ratios						Apparent age (Ma)						Concordance
		$^{207}\text{Pb}/^{206}\text{Pb}$	1 $\sigma$	$^{207}\text{Pb}/^{235}\text{U}$	1 $\sigma$	$^{206}\text{Pb}/^{238}\text{U}$	1 $\sigma$	$^{207}\text{Pb}/^{206}\text{Pb}$	1 $\sigma$	$^{207}\text{Pb}/^{235}\text{U}$	1 $\sigma$	$^{206}\text{Pb}/^{238}\text{U}$	1 $\sigma$	
Sample CR-01 (Granite porphyry)														
LIB CR01-01	MZ	0.0586	0.0016	0.8697	0.0244	0.1073	0.0010	550	54.62	635	13.27	657	6.08	96%
LIB CR01-02	MZ	0.0639	0.0016	0.9178	0.0239	0.1039	0.0009	739	53.70	661	12.68	637	5.15	96%
LIB CR01-03	HAZ	0.0619	0.0017	0.8942	0.0232	0.1047	0.0009	672	60.02	649	12.43	642	5.00	98%
LIB CR01-04	HAZ	0.0627	0.0013	0.9197	0.0185	0.1059	0.0007	698	42.59	662	9.78	649	4.31	97%
LIB CR01-05	HAZ	0.0622	0.0015	0.9003	0.0206	0.1049	0.0008	680	50.00	652	11.01	643	4.85	98%
LIB CR01-06	HAZ	0.0579	0.0016	0.8617	0.0243	0.1073	0.0008	528	52.77	631	13.26	657	4.89	95%
LIB CR01-07	MZ	0.0611	0.0022	0.8821	0.0313	0.1049	0.0009	643	79.62	642	16.91	643	5.55	99%
LIB CR01-08	MZ	0.0610	0.0018	0.9090	0.0257	0.1082	0.0009	639	62.95	657	13.69	662	5.39	99%
LIB CR01-10	MZ	0.0637	0.0018	0.9291	0.0265	0.1054	0.0009	731	59.25	667	13.95	646	5.47	96%
LIB CR01-11	HAZ	0.0617	0.0014	0.9025	0.0200	0.1057	0.0008	661	48.15	653	10.68	648	4.71	99%
LIB CR01-13	MZ	0.0590	0.0017	0.8711	0.0249	0.1066	0.0010	569	61.87	636	13.53	653	5.64	97%
LIB CR01-14	HAZ	0.0595	0.0016	0.8806	0.0239	0.1072	0.0009	583	59.25	641	12.90	656	5.00	97%
LIB CR01-15	HAZ	0.0624	0.0014	0.9248	0.0208	0.1071	0.0009	687	46.29	665	11.00	656	5.54	98%
LIB CR01-16	MZ	0.0619	0.0018	0.9272	0.0265	0.1081	0.0009	672	61.11	666	13.95	662	5.18	99%
LIB CR01-18	MZ	0.0626	0.0017	0.9155	0.0247	0.1058	0.0009	694	57.40	660	13.11	648	5.13	98%
LIB CR01-19	MZ	0.0613	0.0017	0.8816	0.0237	0.1041	0.0009	650	57.40	642	12.80	638	5.43	99%
LIB CR01-20	MZ	0.0643	0.0019	0.9274	0.0260	0.1045	0.0009	754	56.48	666	13.69	641	5.09	96%
LIB CR01-22	MZ	0.0648	0.0019	0.9478	0.0271	0.1059	0.0008	769	61.11	677	14.14	649	4.71	95%
LIB CR01-23	MZ	0.0592	0.0027	0.8588	0.0372	0.1059	0.0012	576	99.99	629	20.33	649	7.19	97%
LIB CR01-24	HAZ	0.0624	0.0019	0.9346	0.0304	0.1081	0.0010	700	58.33	670	15.94	662	5.97	98%
LIB CR01-25	MZ	0.0612	0.0019	0.9198	0.0281	0.1087	0.0009	656	66.66	662	14.88	665	5.12	99%
Sample KB-01 (Potassic altered granite)														
LIB KB01-01	MZ	0.0621	0.0024	0.9131	0.0335	0.1066	0.0012	676	87.95	659	17.81	653	6.71	99%
LIB KB01-02	MZ	0.0624	0.0026	0.8971	0.0369	0.1043	0.0011	687	90.73	650	19.78	639	6.57	98%
LIB KB01-03	MZ	0.0626	0.0019	0.9135	0.0261	0.1057	0.0010	694	69.44	659	13.85	647	5.67	98%
LIB KB01-04	HAZ	0.0671	0.0020	0.9750	0.0272	0.1049	0.0009	843	56.48	691	13.98	643	5.46	92%

LIB KB01-05	MZ	0.0672	0.0026	0.9874	0.0358	0.1070	0.0011	843	81.48	697	18.31	655	6.33	93%
LIB KB01-06	MZ	0.0654	0.0020	0.9359	0.0274	0.1035	0.0012	787	64.81	671	14.38	635	6.92	94%
LIB KB01-07	HAZ	0.0516	0.0082	0.9456	0.1583	0.1091	0.0018	333	264.78	676	82.64	667	10.45	98%
LIB KB01-10	HAZ	0.0606	0.0022	0.9376	0.0294	0.1074	0.0011	633	79.62	672	15.40	658	6.58	97%
LIB KB01-11	MZ	0.0597	0.0018	0.8716	0.0266	0.1053	0.0010	591	66.66	636	14.44	646	5.97	98%
LIB KB01-12	MZ	0.0609	0.0018	0.8881	0.0262	0.1052	0.0011	635	62.95	645	14.08	645	6.60	99%
LIB KB01-13	HAZ	0.0596	0.0023	0.9413	0.0308	0.1067	0.0010	591	83.32	674	16.10	654	5.75	97%
LIB KB01-14	IZ	0.0663	0.0019	0.8419	0.0230	0.0919	0.0008	817	61	832	12.67	867	4.97	90%
LIB KB01-15	MZ	0.0592	0.0016	0.8625	0.0227	0.1049	0.0009	576	59.25	631	12.40	643	5.18	98%
LIB KB01-16	HAZ	0.0611	0.0019	0.8759	0.0261	0.1034	0.0009	643	66.66	639	14.13	634	5.30	99%
LIB KB01-17	MZ	0.0606	0.0023	0.8996	0.0333	0.1071	0.0011	633	79.62	652	17.80	656	6.18	99%
LIB KB01-18	IZ	0.0693	0.0019	1.5511	0.0404	0.1612	0.0013	906	55.56	951	16.10	963	7.26	98%
LIB KB01-19	MZ	0.0586	0.0025	0.8903	0.0374	0.1097	0.0013	554	92.58	647	20.10	671	7.63	96%
LIB KB01-20	HAZ	0.0613	0.0024	0.9312	0.0346	0.1099	0.0011	650	85.17	668	18.18	672	6.27	99%
LIB KB01-21	MZ	0.0629	0.0026	0.9223	0.0382	0.1062	0.0014	706	89.65	664	20.18	651	8.13	98%
LIB KB01-22	MZ	0.0617	0.0020	0.8902	0.0287	0.1043	0.0011	661	70.36	646	15.42	640	6.68	98%
LIB KB01-23	HAZ	0.0628	0.0018	0.9111	0.0253	0.1048	0.0009	702	61.11	658	13.47	642	5.25	97%
LIB KB01-24	MZ	0.0631	0.0016	0.9243	0.0235	0.1058	0.0011	722	55.55	665	12.40	648	6.59	97%
LIB KB01-25	MZ	0.0606	0.0017	0.9101	0.0251	0.1084	0.0010	633	61.10	657	13.36	664	5.62	99%

Note:

MZ = Magmatic zircon.

HAZ = Hydrothermally-altered zircon.

IZ = Inherited zircon

All of these abbreviations are also applied to the tables below.

**Table 3. Zircon in situ Lu-Hf isotopic compositions for the Libata granites**

Spot No	Type	$^{176}\text{Lu}/^{177}\text{Hf}$	$^{176}\text{Yb}/^{177}\text{Hf}$	$^{176}\text{Hf}/^{177}\text{Hf}$	$\pm 1\sigma$	Age (Ma)	$\epsilon\text{Hf}(t)$	TDM(Ma)	TDM2(Ma)	$f\text{Lu}/\text{Hf}$
Sample CR-01 (Granite porphyry)										
CR-01-01	MZ	0.000691	0.029189	0.282494	0.000013	657	4.37	1063	1311	-0.98
CR-01-02	MZ	0.000756	0.032046	0.282531	0.000012	637	5.21	1013	1242	-0.98
CR-01-03	HAZ	0.000573	0.023931	0.282525	0.000013	642	5.17	1017	1249	-0.98
CR-01-04	HAZ	0.000673	0.028206	0.282519	0.000012	643	4.94	1028	1264	-0.98
CR-01-05	HAZ	0.000735	0.031256	0.282519	0.000011	657	5.24	1029	1256	-0.98
CR-01-06	HAZ	0.000600	0.024872	0.282502	0.000014	648	4.50	1049	1296	-0.98
CR-01-07	MTZ	0.000730	0.030653	0.282529	0.000014	421	0.47	1015	1378	-0.98
CR-01-08	HAZ	0.000845	0.036266	0.282534	0.000013	656	5.69	1012	1227	-0.97
CR-01-09	MZ	0.000610	0.025232	0.282522	0.000014	665	5.56	1022	1242	-0.98
CR-01-10	MZ	0.000720	0.030418	0.282534	0.000014	638	5.34	1009	1235	-0.98
CR-01-11	MZ	0.000654	0.027413	0.282514	0.000013	657	5.10	1034	1265	-0.98
CR-01-12	MZ	0.001012	0.044225	0.282545	0.000014	665	6.21	1000	1201	-0.97
Sample KB-01 (Potassic altered granite)										
KB-01-01	MZ	0.000706	0.029589	0.282539	0.000016	653	5.85	1001	1214	-0.98
KB-01-02	HAZ	0.001162	0.046562	0.282676	0.000017	643	10.31	819	923	-0.97
KB-01-03	HAZ	0.001227	0.054186	0.282579	0.000015	655	7.10	958	1137	-0.96
KB-01-04	MZ	0.000716	0.030064	0.282544	0.000015	667	6.34	994	1194	-0.98
KB-01-05	HAZ	0.000657	0.028083	0.282676	0.000013	658	10.85	808	901	-0.98
KB-01-06	HAZ	0.000797	0.033398	0.282572	0.000014	654	7.01	958	1142	-0.98
KB-01-07	MZ	0.000574	0.019880	0.282593	0.000013	656	7.90	922	1087	-0.98
KB-01-08	IZ	0.000804	0.033752	0.281972	0.000012	963	-7.53	1791	2293	-0.98
KB-01-09	MZ	0.000639	0.026938	0.282521	0.000015	651	5.20	1025	1254	-0.98
KB-01-10	MZ	0.000554	0.019038	0.282580	0.000013	640	7.09	940	1126	-0.98
KB-01-11	HAZ	0.000843	0.029512	0.282590	0.000012	642	7.39	933	1108	-0.97
KB-01-12	MZ	0.000927	0.039216	0.282591	0.000012	664	7.85	934	1096	-0.97

Note:

MZ = Magmatic zircon.

MTZ = Metamict zircon

HAZ = Hydrothermally-altered zircon.

IZ = Inherited zircon